ADVANCING EARTH AND SPACE SCIENCE

JGR Space Physics

RESEARCH ARTICLE

10.1029/2019JA026694

This article is a companion to Vadas et al. (2019), https://doi.org/10.1029/2019JA026693.

Key Points:

- Upward- and downward-propagating tertiary GWs are generated in the mesosphere and thermosphere during strong mountain wave events
- The tertiary GWs have concentric ring structure and are generated by body forces created from the dissipation of secondary GWs
- Some of the tertiary gravity waves have horizontal phase speeds >300 m/s, which precludes a source in the lower/middle atmosphere

Correspondence to:
S. L. Vadas,
vasha@nwra.com

Citation:
Vadas, S. L., & Becker, E. (2019). Numerical modeling of the generation of tertiary gravity waves in the mesosphere and thermosphere during strong mountain wave events over the Southern Andes. *Journal of Geophysical Research: Space Physics*, *124*, 7687–7718. https://doi.org/10.1029/2019JA026694

Received 7 MAR 2019
Accepted 5 JUN 2019
Accepted article online 11 JUN 2019
Published online 17 SEP 2019

Numerical Modeling of the Generation of Tertiary Gravity Waves in the Mesosphere and Thermosphere During Strong Mountain Wave Events Over the Southern Andes

Sharon L. Vadas[1] and Erich Becker[2]

[1]Northwest Research Associates, Boulder, CO, USA, [2]Leibniz Institute of Atmospheric Physics, Kühlungsborn, Germany

Abstract We investigate the effects on the mesosphere and thermosphere from a strong mountain wave (MW) event over the wintertime Southern Andes using a gravity wave (GW)-resolving global circulation model. During this event, MWs break and attenuate at $z \sim 50$–80 km, thereby creating local body forces that generate large-scale secondary GWs having concentric ring structure with horizontal wavelengths $\lambda_H = 500$–2,000 km, horizontal phase speeds $c_H = 70$–100 m/s, and periods $\tau_r \sim 3$–10 hr. These secondary GWs dissipate in the upper mesosphere and thermosphere, thereby creating local body forces. These forces have horizontal sizes of 180–800 km, depending on the constructive/destructive interference between wave packets and the overall sizes of the wave packets. The largest body force is at $z = 80$–130 km, has an amplitude of ~2,400 m/s/day, and is located ~1,000 km east of the Southern Andes. This force excites medium- and large-scale "tertiary GWs" having concentric ring structure, with λ_H increasing with radius from the centers of the rings. Near the Southern Andes, these tertiary GWs have $c_H = 120$–160 m/s, $\lambda_H = 350$–2,000 km, and $\tau_r \sim 4$–9 hr. Some of the larger-λ_H tertiary GWs propagate to the west coast of Africa with very large phase speeds of $c_H \simeq 420$ m/s. The GW potential energy density increases exponentially at $z \sim 95$–115 km, decreases at $z \sim 115$–125 km where most of the secondary GWs dissipate, and increases again at $z > 125$ km from the tertiary GWs. Thus, strong MW events result in the generation of medium- to large-scale fast tertiary GWs in the mesosphere and thermosphere via this multistep vertical coupling mechanism.

1. Introduction

Wind flow over orography excites mountain waves (MWs) Fritts & Alexander, 2003; Holton, 1992; McFarlane, 1987). If the wind is constant in time and the flow is linear, the ground-based phase speed of a MW, c_H, is zero, and the solution is steady-state. MWs have been observed over the Southern Andes and the Antarctic Peninsula with the Cryogenic Infrared Spectrometers and Telescopes for the Atmosphere (Eckermann & Preusse, 1999; Ern et al., 2004), the Upper Atmosphere Research Satellite Microwave Limb Sounder (Jiang et al., 2002; Wu & Jiang, 2002), the Atmospheric Infrared Sounder (Alexander & Teitelbaum, 2007, 2011; Gong et al., 2012; Hoffmann & Alexander, 2009; Wu et al., 2006), the High Resolution Dynamics Limb Sounder and the Sounding of the Atmosphere using Broadband Emission Radiometry (SABER; Alexander et al., 2008; Ern et al., 2011; Liu et al., 2019), the meteorological program of the Global Positioning System (Tsuda et al., 2000), GPS radio occultation (de la Torre & Alexander, 2005), OH airglow imagers (Smith et al., 2009), and superpressure balloons (Plougonven et al., 2008; Vincent et al., 2007; Walterscheid et al., 2016). They have also been observed over New Zealand in the Deep Propagating Gravity Wave Experiment (Bossert et al., 2015, 2017; Eckermann et al., 2016; Fritts et al., 2016; Heale et al., 2017) and near McMurdo Station in Antarctica with superpressure balloons and Atmospheric Infrared Sounder (Vincent et al., 2007; Hoffmann et al., 2013; Hendricks et al., 2014).

MWs and their effects can be modeled in the winter stratosphere and mesosphere-lower thermosphere (MLT) by high-resolution global circulation models which resolve atmospheric gravity waves (GWs). Sato et al. (2012) found stratospheric MW hot spots leeward of the Southern Andes during winter. They showed a correlation between downward energy flux in the stratosphere and orographic GW activity over the Southern Andes. They postulated that this might be due to partial wave reflection from the changing buoyancy frequency or to nonlinear processes (i.e., small-scale secondary GWs created from wave breaking), although neither possibility was deemed as entirely satisfactory. Watanabe et al. (2006) also found orographic GWs near McMurdo in July, thereby confirming their creation from downslope winds there. Recently, Becker and Vadas (2018) and Vadas and Becker (2018; hereafter BV18 and VB18, respectively) analyzed GWs in the stratosphere and mesosphere in the southern winter hemisphere using the high-resolution, GW-resolving Kühlungsborn Mechanistic general Circulation Model (KMCM) that resolves GWs down to $\lambda_H = 165$ km. They found that westward MWs were created by eastward flow over the Southern Andes, Antarctic Peninsula, and McMurdo Station. During large events triggered by tropospheric Rossby waves, MWs propagated to the stratopause region where they broke and created temporally and spatially dependent wave drag (called local body forces). (Note that a local body force is a spatially and temporally localized horizontal acceleration of the background flow.) These events preceded strong GW events in the MLT. Importantly, BV18 and VB18 found that the GWs in the MLT propagated eastward, westward, northward, and southward, with peak values of $c_H \sim 60$m/s. They identified these GWs as secondary GWs from local body forces due to MW breaking in the stratopause region. They also found that some of the secondary GWs broke and dissipated in the MLT. Note that small-scale secondary GWs are also created from nonlinear processes accompanying wave breaking. However, because these latter secondary GWs have smaller horizontal scales than the primary GWs and have small phase speeds, most do not propagate very far before being "reabsorbed" into the fluid in the transition to turbulence; therefore, these latter GWs likely do not transfer significant amounts of momentum and energy into the thermosphere. For the remainder of this paper, we refer to "secondary GWs" as the former, larger-scale GWs generated by local body forces.

Vadas et al. (2018) calculated the theoretical spectra of secondary GWs from MW breaking during the winter over McMurdo. They found that these spectra are quite broad and have $\lambda_H \sim 500$ to thousands of kilometers, $\lambda_z \sim 10$–150 km, and $c_H \sim 50$–250 m/s. They also found that secondary GWs form "fishbone" structures in $z - t$ plots of the temperature and wind perturbations. VB18 analyzed the wintertime KMCM data over McMurdo during large MW events. They found that fishbone structures were common in the stratopause region and that these structures contained upward- and downward-propagating secondary GWs with $\lambda_H \sim 1,000$–3,000 km and $c_H \sim 40$–70 m/s. Detailed analysis showed that these GWs were excited by horizontal body forces that were created by the breaking of MWs near the stratopause.

Recent observational evidence supports the occurrence of secondary GWs in the winter MLT. GW momentum flux estimates based on meteor radar measurements east of the Southern Andes revealed a significant vertical flux of eastward momentum which could not be explained by nonorographic tropospheric GWs because of critical level filtering by the strong polar vortex (de Wit et al., 2017). Indeed, de Wit et al. (2017) argued that these fluxes were secondary GWs excited from MW breaking over the Southern Andes. Using SABER data, Liu et al. (2019) showed that GW amplitudes in the Southern Hemisphere during the wintertime peak over the Southern Andes, with a westward tilt of the maximum with increasing altitude at $z > 65$ km; they argued that these GWs were likely secondary GWs from MW breaking. Finally, several fishbone structures were identified in lidar data at McMurdo near the winter stratopause and were shown to contain secondary GWs (Vadas et al., 2018). As corroboration of these results, analysis of wintertime lidar data at McMurdo inferred that λ_H of the GWs was much larger in the MLT than in the stratosphere (Chen et al., 2013; Chen & Chu, 2017; Zhao et al., 2017), in excellent agreement with model results (BV18; VB18).

Because the secondary GW spectrum excited by a body force is broad (Fritts et al., 2006; Vadas & Fritts, 2002; Vadas et al., 2003, 2018), it is expected that some of the smaller-amplitude secondary GWs with intrinsic horizontal phase speeds of $c_{IH} \sim 100$m/s can propagate above the turbopause to $z \sim 130$ km (Vadas, 2007). Above the turbopause, GWs dissipate from kinematic viscosity, thermal diffusivity, ion drag, wave-induced diffusion, and wave breaking (if the GW amplitudes are large enough), with kinematic viscosity (ν) and thermal diffusivity ($\nu/$ Pr, where Pr ~ 0.62 is the Prandtl number) being the most important dissipation mechanism for linear-amplitude GWs with observed periods of $\tau_r <$ few hours (DelGenio & Schubert, 1979; Gossard & Hooke, 1975; Heale et al., 2017; Hickey & Cole, 1988; Lund & Fritts, 2012; Miyoshi & Fujiwara, 2008; Pitteway & Hines, 1963; Yiğit et al., 2008, 2009; Vadas, 2007; Vadas & Fritts, 2004, 2005). Because ν grows exponentially with altitude, every GW eventually dissipates from viscosity, although the height where this occurs depends sensitively on the intrinsic period, τ_{Ir}, and λ_z (Vadas, 2007; Vadas & Liu, 2009). In particular, GWs with smaller (larger) λ_z and c_{IH} dissipate at lower (higher) altitudes (Pitteway & Hines, 1963; Vadas, 2007; Volland, 1969), as has been observed for λ_z (Djuth et al., 1997, 2004; Oliver et al., 1997).

Many GWs from deep convection can propagate directly into the thermosphere, where they dissipate and create local body forces (Vadas, 2013; Vadas & Liu, 2009; 2013). These body forces peak at $z \sim 140$–200 km with amplitudes of ∼0.2–1.0 m/s^2 over spatially localized regions of ∼100–1,500 km and time scales of ∼10–30 min and (1) excite a broad spectrum of secondary GWs having $\lambda_H \sim$ 100–4,000 km and $\underline{c_H} \sim$ 100–500 m/s and (2) create counterrotating cells in the neutral mean flow with amplitudes of $\overline{u'_H} \sim$ 50–200 m/s (Vadas & Crowley, 2010; Vadas & Liu, 2009, 2013; Vadas et al., 2014). Vadas and Liu (2009) showed that a low-latitude convective plume created secondary GWs with $\rho'/\bar{\rho} \sim$ 4–5% at $z \sim 400$ km and [O] perturbations of ∼2% at $z = 300$ km, in agreement with low Kp CHAMP and DE2 satellite observations, respectively (Bruinsma & Forbes, 2008; Hedin & Mayr, 1987; Mayr et al., 1990). Because deep convection is the main source of GWs at low latitudes, Vadas and Liu (2009) concluded that most of the low latitude quiet-time (i.e., low Kp) $\rho'/\bar{\rho}$ and [O] perturbations measured by these satellites were likely secondary GWs generated by the thermospheric body forces created from the dissipation of primary GWs from deep convection. Vadas et al. (2014) modeled the GWs from deep convection worldwide for 13 days in the years 2000 and 2009 and found that the dissipation of these GWs significantly changed the wind and temperature structure at $z > 150$ km in the thermosphere. In particular, their dissipation created "jet"-like eastward mean wind perturbations at low latitudes of ∼50–100 m/s and wesward mean wind perturbations at midlatitudes as part of the larger-scale clockwise and counterclockwise mean wind circulations created by this fundamental process. Thus, the dissipation of GWs from deep convection was found to significantly alter the dynamics of the thermosphere.

Given the results of GWs from deep convection discussed in the previous paragraph (e.g., Vadas & Liu, 2009, 2013), we hypothesize that the dissipation of secondary GWs from MW breaking creates significant body forces in the upper mesosphere and thermosphere. Because these body forces are localized in space and time over scales of order (1) the size of the breaking/attenuating wave packet or (2) the region where constructive/destructive interference occurs between GW packets (Vadas & Crowley, 2010), we expect these upper-mesospheric and thermospheric body forces to excite "tertiary" GWs via the same mechanism as originally proposed by Vadas et al. (2003); a local body force creates an imbalance in the background flow, and the flow responds by radiating GWs and creating a pair of counterrotating cells in the mean horizontal wind.

The purpose of this paper is to show that this hypothesis is true, that is, that tertiary GWs are excited in the upper mesosphere and thermosphere following strong MW events over the Southern Andes. For this purpose, we perform a model study based on the KMCM extended to $z \sim 200$ km. A companion paper determines the intrinsic properties, propagation directions, and possible sources of GWs extracted from the Gravity Field and Ocean Circulation Explorer (GOCE) satellite data at $z \simeq 277$ km on 5 July 2010 over the Southern Andes (Vadas et al., 2019). In section 2, we describe the KMCM. Section 3 presents an overview of our results. We analyze the results of this model during 9 days in July in section 4. A discussion and our conclusions are contained in sections 5 and 6, respectively.

2. Description of the KMCM Model

The model we use for this study is the KMCM, which is a high-resolution, GW-resolving, hydrostatic, free-running global circulation model. It is based on a standard spectral dynamical core with a terrain-following hybrid vertical coordinate. We use a triangular spectral truncation at total horizontal wave number 240. The grid spacing is ∼65 km in the horizontal direction. In the vertical direction, the grid spacing is ∼600 m at $z \leq 100$ km, ∼2 km at $z \sim 130$ km, and ∼4 km at $z \sim 165$ km. The smallest GW horizontal wavelength resolvable is $\lambda_H = 165$ km at any altitude. Explicit computations of radiation and the tropospheric moisture cycle are included (Becker, 2017; Becker et al., 2015). Land-sea contrasts are included via orography and land-sea masks (albedo, surface humidity, heat capacity, and roughness length). This includes a simple slab ocean model and a closed surface energy budget. Subgrid-scale parameterizations consist of (1) a local boundary diffusion scheme, (2) a simple tropospheric moist convection scheme, and (3) a Smagorinsky-type horizontal and vertical diffusion scheme for the whole atmosphere, with both diffusion coefficients dependent on the Richardson number, R_i, that give rise to wave damping when $R_i \leq 0.25$ (Becker, 2009; BV18). All subgrid-scale momentum diffusion and frictional heating terms are derived from a symmetric stress tensor (e.g., Becker, 2017). This also includes weak hyperdiffusion (Brune & Becker, 2013).

The KMCM explicitly simulates momentum and energy deposition from GWs, including their spatial and temporal intermittency. This occurs because resolved GW packets that become dynamically unstable are damped by the subgrid-scale turbulent diffusion. Note that subgrid-scale diffusion is necessary for creating the wave-mean flow interaction, as is evident from the Wentzel-Kramers-Brillouin (WKB) solution for GWs damped by diffusion (e.g., Becker, 2012; Lindzen, 1981).

In this study, we employ a model version that is similar to the one used in BV18, except that we extend the model into the thermosphere. The KMCM here has 220 full model layers (T240L220) up to $\sim 9 \times 10^{-7}$ hPa ($z \sim$ 200 km). The sponge layer starts at $z >$ 165 km and is due to linear harmonic horizontal diffusion. Our simple model thermosphere utilizes analytic formulas, Equations (3)–(4) of Vadas (2007), to specify the gas constant and specific heat capacities as functions of pressure. The KMCM also utilizes a simple ion drag scheme (Hong & Lindzen, 1976). After spinning up, the model was run for 10 days in the southern hemisphere winter. We chose to run the model during July when the polar night jet was well-established in the southern hemisphere. This allowed the MWs to propagate to the stratopause region before breaking (e.g., Liu et al., 2019; Trinh et al., 2018), thereby resulting in strong MW events and secondary GW generation (BV18; VB18). The model data were saved every Δt = 45 min. We interpolate these data to an altitudinal grid having a fixed vertical grid spacing of Δz = 2 km for $z \geq$ 4 km.

3. Overview: Strong MW Event Over the Southern Andes

To motivate why we perform this study, we first show an overview figure that contains snapshots of the atmosphere from the lower stratosphere to the thermosphere during a strong MW event over the Southern Andes. Figure 1 shows stereographic projections of the vertical velocity, w, at various times from 0 to 10:30 UT on 23 July at altitudes of z = 20 to 160 km. MWs are visible over the Southern Andes in the lower stratosphere (i.e., at z = 20 km). (The Southern Andes is located south of the Llullaillaco Volcano at 24° S and 68° W.) The northwest-southeast tilt of the MW phase lines near Tierra del Fuego in Figure 1a likely occurs because the topography is curved as it follows the coastline (Preusse et al., 2002). The MWs are also located over the Southern Andes at z = 40 km in Figure 1b, but some of the MWs near Tierra del Fuego have drifted significantly southeastward over the South Atlantic Ocean, as is common at this latitude and altitude (Alexander & Teitelbaum, 2011; Preusse et al., 2002; Sato et al., 2012; Wu & Eckermann, 2008).

At z = 90 km in the mesosphere in Figure 1c, the MWs appear to be mostly absent. Medium-scale GWs spanning a wide region are now visible. In addition, GWs having partial concentric ring structures are visible over and east of the Southern Andes. The estimated centers of these rings are located near the southern tip of South America. There are also medium-scale GWs and GWs having partial concentric ring structures at z = 100 km in Figure 1d. The estimated centers of these rings appear to be located ~100–500 km east of the Southern Andes.

In the thermosphere (i.e., at z = 130 and 160 km in Figures 1e and 1f), well-defined concentric rings of GWs (spanning angles of nearly 360°) are stunningly visible over South America, the Atlantic and Pacific Oceans, the Drake Passage, and the Antarctic Peninsula. These GWs have very large amplitudes of $w \sim$ 10 m/s in the vicinity of South America at $z \sim$ 160 km. They also span a large horizontal area, with some of the GWs propagating to Africa and Brazil at z = 160 km. The centers of these concentric rings are located a few hundred kilometers east of the tip of South America at ~300° E (i.e., ~60° W) and ~50° S. We note that the horizontal wavelengths, λ_H, of the large-scale concentric GWs appear to increase significantly with distance from the ring centers at z = 160 km.

We now perform detailed analyses of the model data at many different altitudes and times in section 4 in order to better understand and describe the features seen in Figure 1.

4. Response of the Atmosphere to Strong MW Events During the Winter Over the Southern Andes

4.1. MWs Over the Southern Andes

In order to determine what creates the concentric rings of GWs in the thermosphere, we first need to understand the propagation, breaking, and attenuation of the MWs over the Southern Andes. Figure 2 shows the temperature T and the zonal (u), meridional (v), and vertical (w) velocities during 15–24 July at 73.8° W (286.2° E) and 50.625° S over the Southern Andes. The stratopause is located at $z \sim$ 50 km. At $z >$ 100 km, the temperature increases to $T \sim$ 600 K at $z \sim$ 170 km. The polar night jet is very strong at this location, with a magnitude of $u \sim$ 150–200 m/s at $z \sim$ 40–70 km. Although the semidiurnal tide is generally dominant in the MLT in u and v, the diurnal tide begins to become important at $z >$ 150 km because of in situ

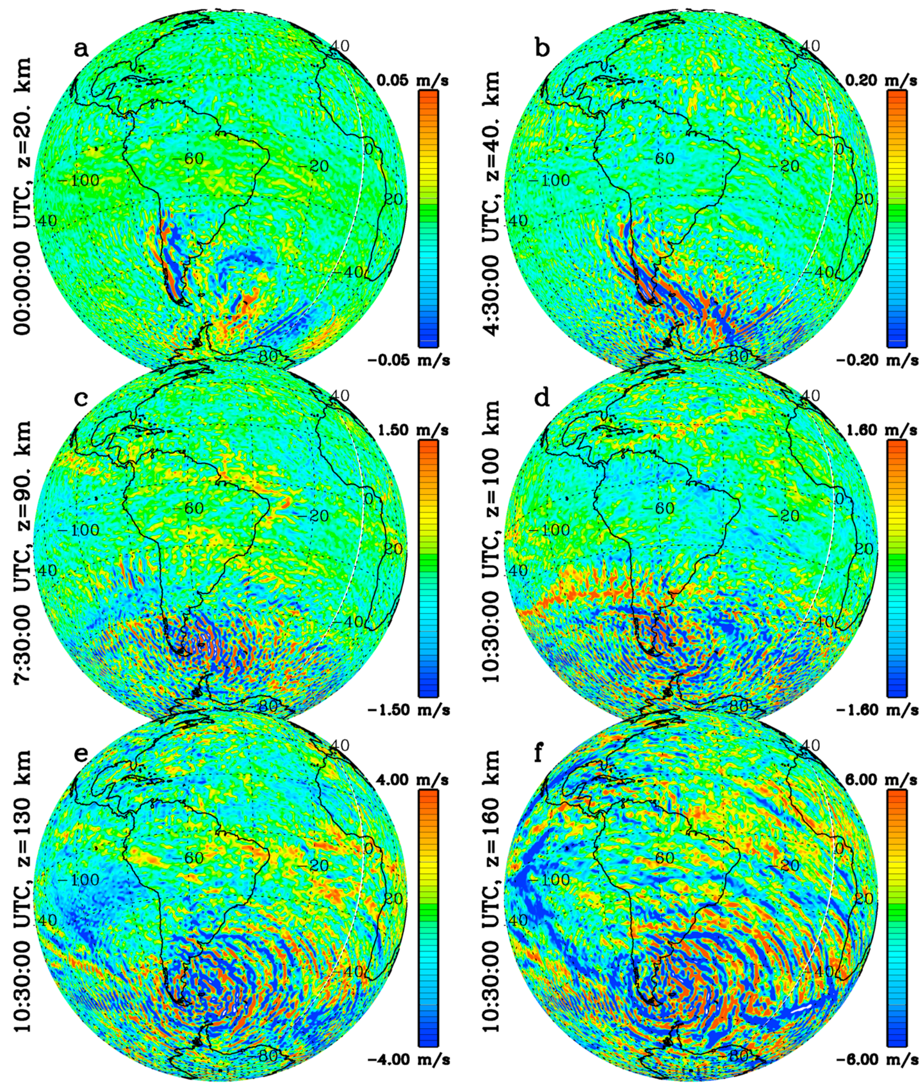

Figure 1. The vertical velocity w on 23 July at (a–f) $z = 20$, 40, 90, 100, 130, and 160 km at 00:00, 4:30, 7:30, 10:30, 10:30, and 10:30 UT, respectively.

generation by solar absorption. Strong MW events (whereby the phases at a particular height are approximately constant in time) are seen in the vertical velocity w up to altitudes of $z \sim 70$ km during 18.25–19, 20–21.5, and 23–24 July. (Here 18.25 July refers to 6:00 UT on 18 July.) At higher altitudes, GWs with periods of $\tau_r \sim 1$–4 hr are visible in w. They are also present in T, u, and v but are more difficult to see until the tides are removed (see below).

Figure 3 shows w at $z = 20$, 60, and 80 km at 49.875° S as a function of longitude and time. Here we only show the data on 20–24 July in order to focus on the days prior to the strong MW event on 23–24 July (shown in Figure 1). The Southern Andes are located at ∼280–292° E at this latitude. Quasi-stationary medium-scale MWs with $\lambda_H \sim 230$–420 km are present at $z = 20$ and 60 km most of the time during 20–24 July. At $z = 80$ km, however, the medium-scale MWs are mostly absent; this is especially true after 22 July, when small-scale GWs dominate. These small-scale GWs may be a combination of (1) small-scale MWs with initially tiny amplitudes that propagate to the mesosphere before dissipating and/or (2) small-scale secondary GWs created from the breaking and attenuation of the medium-scale MWs.

A midfrequency GW with $|\lambda_z| \ll 2\pi\mathcal{H}$ satisfies the GW dispersion relation

$$\omega_{Ir}^2 \simeq \left(\frac{k_H N_B}{m}\right)^2, \tag{1}$$

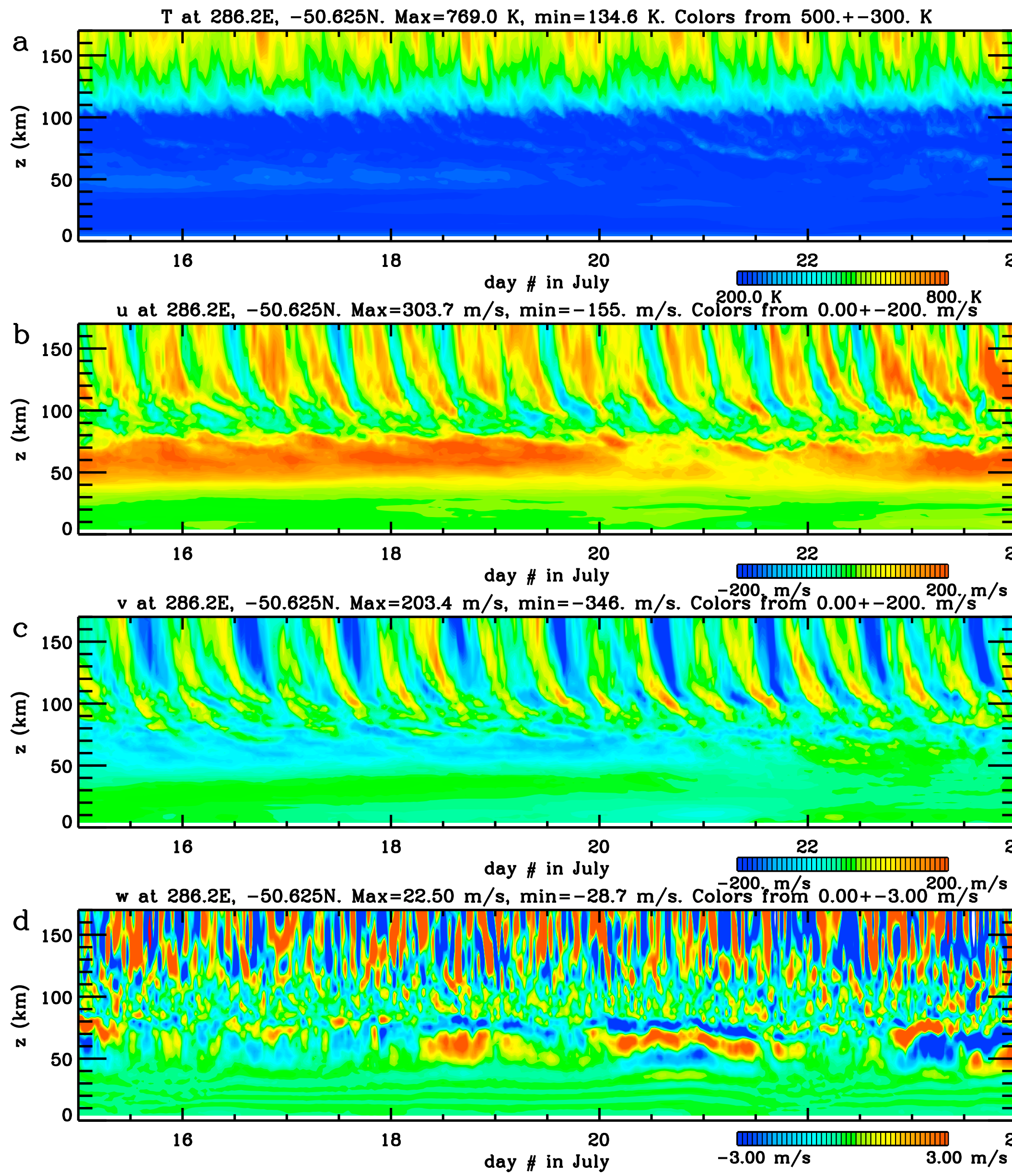

Figure 2. Temperature T (a), zonal velocity u (b), meridional velocity v (c), and vertical velocity w (d) during 15–24 July at 286.2° E (i.e., 73.8° W) and 50.625° S. Maximum and minimum values are shown at the top of each panel.

where ω_{Ir} is the intrinsic frequency; $\mathcal{H}$ is the density scale height; N_B is the buoyancy frequency; $k_H = \sqrt{k^2 + l^2} = 2\pi/\lambda_H$; k, l, and m are the zonal, meridional, and vertical wave numbers, respectively; and $m = 2\pi/\lambda_z$. The intrinsic horizontal phase speed of a GW is

$$c_{IH} = \omega_{Ir}/k_H = c_H - U_H, \tag{2}$$

where $c_H = \omega_r/k_H$ is the observed horizontal phase speed, ω_r is the observed wave frequency,

$$U_H = (k\bar{U} + l\bar{V})/k_H \tag{3}$$

is the background horizontal wind along the direction of GW propagation, and $\bar{U}$ and $\bar{V}$ are the zonal and meridional components of the background wind, respectively. Using these relations, equation (1) can be rewritten as

$$|\lambda_z| = \frac{2\pi|c_H - U_H|}{N_B}. \tag{4}$$

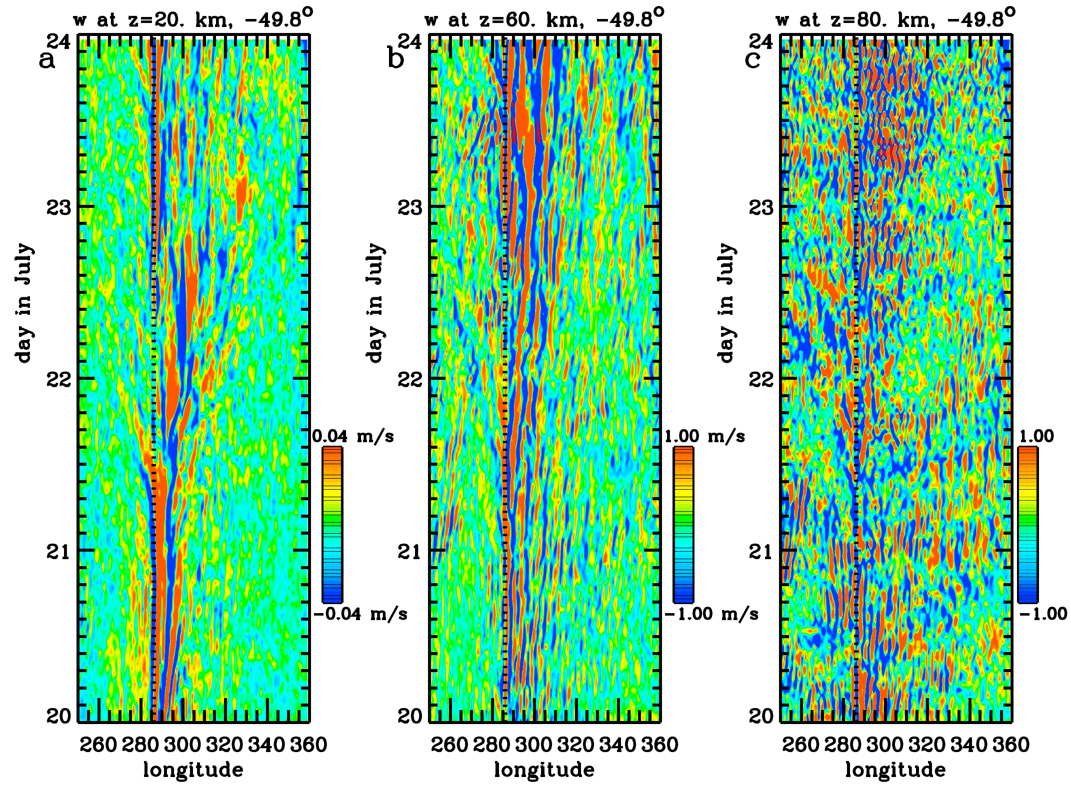

Figure 3. The vertical velocity, w (color contours), at 49.875° S as a function of longitude and time at $z = 20$ km (a), 60 km (b), and 80 km (c). The dotted lines show the location of 286° E (i.e., 74° W).

If the wind that excites a MW is relatively stationary in time and horizontally uniform, then $c_H \sim 0$. In this case, $|\lambda_z|$ varies with height according to the changes of $|U_H|$ and N_B with altitude:

$$|\lambda_z| = \frac{2\pi|U_H|}{N_B}. \tag{5}$$

For the MWs we study here, the phase lines are oriented approximately north-to-south (see Figure 1a). Thus, these MWs propagate primarily zonally. Therefore, as $\bar{U}$ increases (decreases) with height in the lower (upper) half of the polar night jet (which peaks at $z \sim$ 50–60 km from Figure 2b), the MW $|\lambda_z|$ increases (decreases) from equation (5). The condition for a GW (including a MW) to break from convective instability is

$$\frac{|u'_H|}{|c_H - U_H|} \simeq 0.7 \;\; to \;\; 1.0, \tag{6}$$

where u'_H is the horizontal wind amplitude of the GW (Fritts & Alexander, 2003; Lindzen, 1981). Substituting equation (4) into equation (6), the condition for convective instability (using the value "0.7" from equation (6)) is

$$|u'_H| \simeq 0.7 \frac{|\lambda_z|}{\tau_B}, \tag{7}$$

where $\tau_B = 2\pi/N_B$ is the buoyancy period. If a GW's amplitude is small, u'_H grows approximately exponentially with altitude because of the exponential decrease in the background density (Hines, 1960). Therefore, equations (5) and (7) show that as $|\lambda_z|$ increases in the lower half of the polar night jet, the MWs can propagate to much higher altitudes before reaching convective instability. In the upper half of the polar night jet, however, $|\lambda_z|$ decreases, thereby causing the MWs to succumb to breaking from convective instability.

We now focus on the strong MW event that occurs on 23–24 July. From Figure 2b, we see that on 23 July, the polar night jet begins at $z \simeq 40$ km, is maximum at $z \simeq 55$ km with $\bar{U} \simeq 150$ m/s, and decreases to zero at higher altitudes. In particular, $\bar{U}$ is negative at $z =$ 80–85 km on 23.0 July; this region descends to

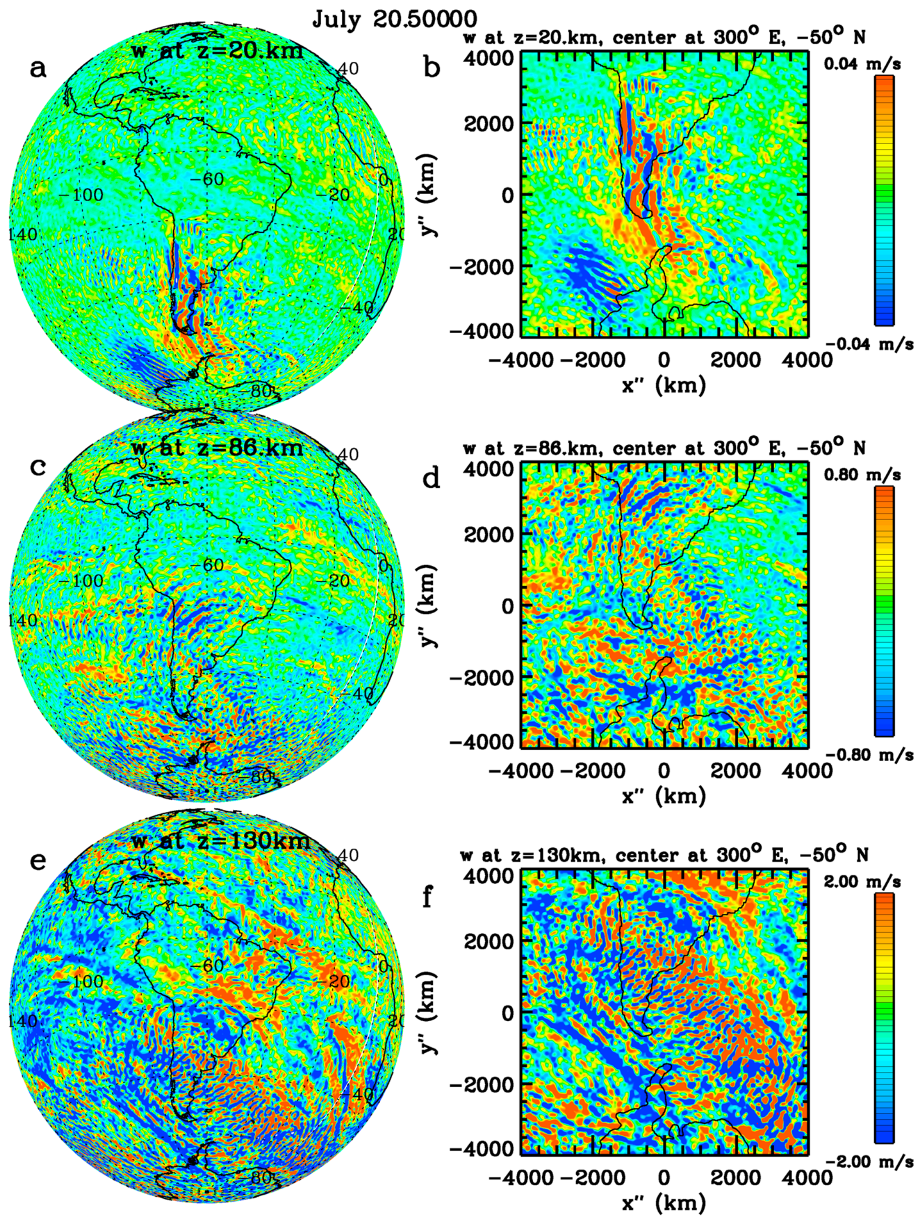

Figure 4. (a,b) The vertical velocity w at z = 20 km on 20.5 July (color contours). (a) Stereographic projection of w. (b) w on a 2-D plane parallel to the Earth's surface at 300° E and 50° S using the transformation from Appendix B of VB18. $x'' = y'' = 0$ is located at 300° E and 50° S. (c,d) Same as (a) and (b) but at z = 86 km. (e,f) Same as (a) and (b) but at z = 130 km.

z = 70–75 km on 24.0 July (likely due to the descent of a tidal phase in time, similar to Eckermann et al., 2016). At the altitude where $\bar{U}$ becomes negative, the MWs reach a critical level whereby $|\lambda_z| \rightarrow 0$ (see equation (5)). From equations (5) and (7), the MWs can propagate easily to $z \simeq 50$ km but will break and attenuate from convective instability at $z \simeq 50$–70 km if their initial amplitudes are large enough. If they survive to higher altitudes, they will break as they approach their critical level.

MW breaking has important dynamical consequences; as the MWs break and attenuate, they deposit their momentum into the background flow in a time-dependent manner. This results in time-dependent, spatially and temporally localized horizontal accelerations of the background flow (i.e., local body forces) in the direction the MWs were propagating (in the intrinsic reference frame) before breaking. These local body forces cause the background flow to become unbalanced, which results in the creation of counterrotating mean wind cells and the generation of secondary GWs (Vadas et al., 2003, 2018). These secondary GWs are created with concentric ring structure, propagate upward and downward away from the body force, have their largest amplitudes in and against the force direction, and propagate in all azimuths except those perpendicular to the force direction. Note that these secondary GWs are created throughout the duration of the body force (e.g., Vadas, 2013; Vadas & Fritts, 2001).

4.2. Transformation of the Model Data to an Equally Spaced Horizontal Grid

Because the distance between longitude grid points in model output decreases rapidly near the pole, it is convenient for analysis purposes to transform the data from geophysical coordinates to Cartestian coordinates on a 2-D plane that is tangent to Earth at the desired central location. This transformation, described in Appendix B of VB18, involves a series of rotations, dot products, and cross products. It establishes x'' and y'' as the new coordinates on this 2-D plane (with $x'' = y'' = 0$ at the central location) and sets the grid spacings on this 2-D plane to be equal: $\Delta x'' = \Delta y''$. The grid cells on this plane are then populated with the interpolated values from the model data for the desired functions (e.g., w or T'). Note that positive x'' (y'') corresponds to the geophysical eastward (northward) directions at the desired central location *only*. This transformation technique enables Fourier filtering in the horizontal directions to isolate, identify, and quantify the parameters of the GWs. Here we choose the central location of our 2-D grid, $x'' = y'' = 0$, to be located at 300° E and 50° S, with $\Delta x'' = \Delta y'' = 20$ km.

Figure 4a shows a stereographic projection of w at $z = 20$ km on 20.5 July, when the MWs were prevalent and stationary over the Southern Andes (see Figure 3a). Figure 4b shows the results of the transformation and interpolation technique described in the previous paragraph at the same time and altitude as in Figure 4a. We see that this transformation technique works quite well and resolves the GWs and small-scale features correctly down to $\lambda_H \simeq 165$ km. This technique also resolves the features correctly out to at least ∼5,700 km from $x'' = y'' = 0$.

Figures 4c and 4d show the corresponding results at $z = 86$ km. Partial concentric rings of GWs with $\lambda_H \sim$ 280–360 km propagate northwestward over the middle part of South America. These rings have an estimated center at $x \sim 1,100$ km and $y \sim 0$ (i.e., at ∼315° E and ∼50° S). As we show in section 4.3, these are secondary GWs generated by the local body forces created from the breaking of the MWs that have been swept downstream from the Southern Andes. In addition, "small-scale" GWs with $\lambda_H \sim$ 165–200 km are present. Figures 4e and 4f shows the corresponding results at $z = 130$ km. Small-scale GWs with $\lambda_H \sim$ 165–200 km dominate the image directly over, surrounding, and southeast of South America. These GWs are likely due to GW breaking. In addition, smaller-amplitude partial concentric rings of GWs with $\lambda_H \sim$ 300–1,200 km propagate northeast over Brazil. These rings have an estimated center at $x \sim -1,100$ km and $y \sim -500$ km (i.e., at ∼285° E and ∼55° S). As we show in section 4.4, these are tertiary GWs generated by local body forces created from the attenuation of secondary GWs.

4.3. Excitation of Secondary GWs

We now focus on the attenuation of MWs, the creation of local body forces, and the excitation of secondary GWs during strong orographic events. Figure 5 shows the density-scaled quantities $T'\sqrt{\bar{\rho}/\bar{\rho}_0}$, $u'\sqrt{\bar{\rho}/\bar{\rho}_0}$, $v'\sqrt{\bar{\rho}/\bar{\rho}_0}$, and $w\sqrt{\bar{\rho}/\bar{\rho}_0}$ on 19–24 July at 286.2° E and 50.625° S. Here the perturbations (denoted by primes) are obtained by removing waves with $\tau_r > 11$ hr via Fourier filtering in order to eliminate the semidiurnal and diurnal tides and planetary waves. Additionally, $\bar{\rho}_0$ is the value of $\bar{\rho}$ at 0° E, 89.625° S, and $z = 4$ km on 15.0 July. Note that w is still the total vertical wind. White arrows show the locations and times for several MW events; these events are easily seen in w, since the phases at a given altitude are approximately constant in time, with alternating positive/negative values with altitude. Strong MW events occur on 20.25–21.5 and 22.75–24.0 July. During the former event and on 22.75–23.5 July, MWs are seen up to $z \sim 80$ km, with decreasing amplitudes above $z \sim 60$–70 km. The situation is more complicated on 23.5–24.0 July, although we do not analyze the wave activity during this period in this paper. Black arrows show the locations and times for several fishbone structures, which are "sideways V's" in $z-t$ plots. Vadas et al. (2018) showed that (1) a fishbone structure (or sideways V's) in a $z-t$ plot occurs when GWs are generated by a local body force; thus, the fishbone structure is the signature of the generated GWs, and (2) the "knee" of a fishbone structure is located at the central altitude of the horizontally displaced local body force that generated it. In Figure 5, the knees of the fishbone structures are located at $z \sim 50$–70 km. This agrees with the result from Figures 3 and 4 that the MWs attenuated at $z < 80$ km.

During the event on 23–24 July, the MWs propagated to $z \sim 50$–70 km before breaking (see Figure 5d). Figure 6 shows the density-scaled quantities at 286.2° E and 50.625° S in the mesosphere and lower

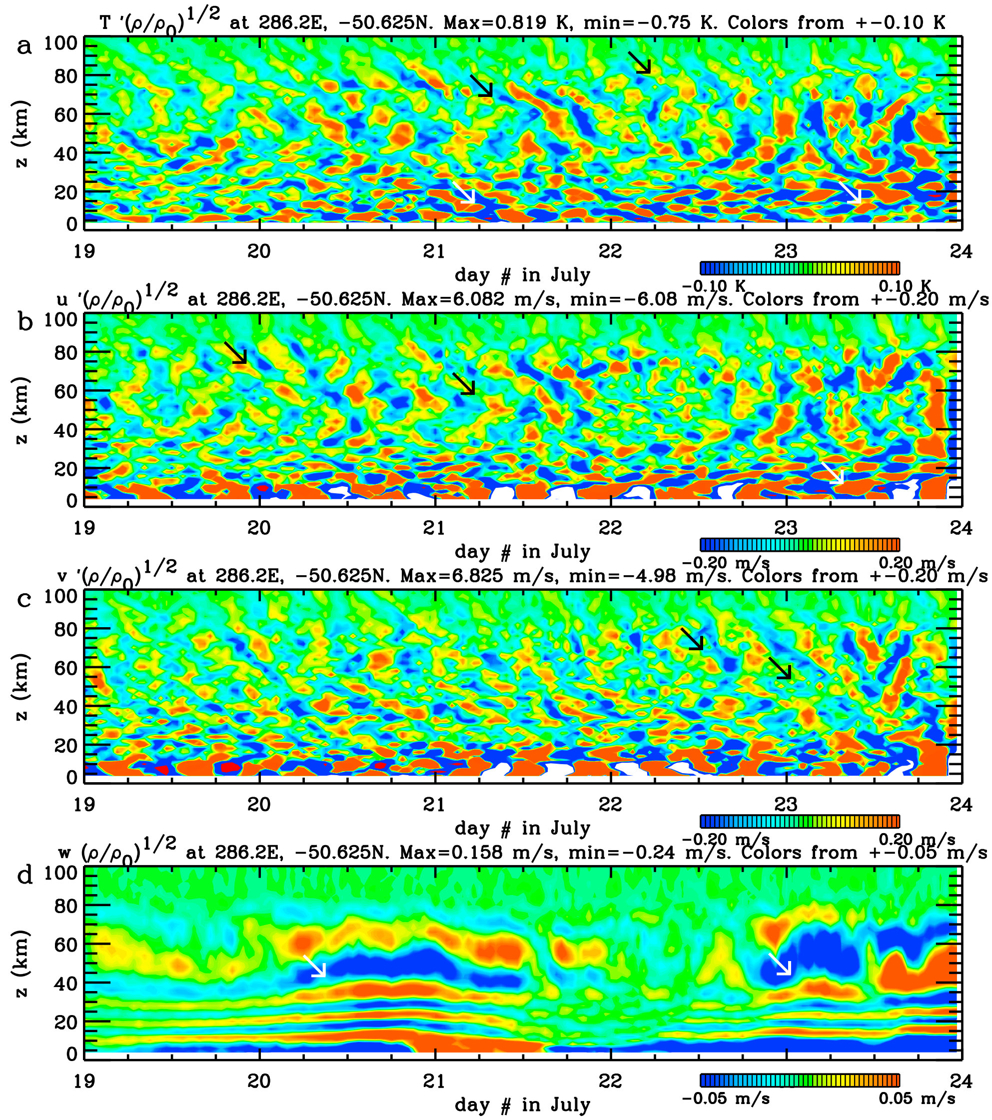

Figure 5. Density scaled quantities on 19–24 July at 286.2° E and 50.625° S. $T'\sqrt{\bar{\rho}/\bar{\rho}_0}$ (a), $u'\sqrt{\bar{\rho}/\bar{\rho}_0}$ (b), $v'\sqrt{\bar{\rho}/\bar{\rho}_0}$ (c), and $w\sqrt{\bar{\rho}/\bar{\rho}_0}$ (d) for $\bar{\rho}_0 = 866.913\,\text{g/m}^3$. White and black arrows show the locations and times for several mountain wave events and fishbone structures, respectively. Here the perturbations (denoted by primes) are obtained via removing waves with $\tau_r > 11$ hr. Maximum and minimum values are shown at the top of each panel.

thermosphere during this event. There is a clear transition in the altitudinal range of $z \sim 60$–80 km, whereby the MWs, and the inertia GWs propagating upward from the troposphere (Figures 6a–6c), disappear and the secondary GWs appear. The MWs can be clearly seen in Figure 6d. The secondary GWs have much smaller amplitudes initially than the MWs; whereas the MWs have a density-weighted amplitude in the vertical wind perturbations of $w\sqrt{\bar{\rho}/\bar{\rho}_0} \sim 0.01$–0.02 m/s at $z \sim 75$ km in Figure 6d, the secondary GWs have $w\sqrt{\bar{\rho}/\bar{\rho}_0} \sim 0.002$–0.005 m/s at $z \sim 80$–85 km. Thus, the initial secondary GW amplitudes are ∼5–10 times smaller than the MW amplitudes in the transition region. However, because of the decrease of the background density in altitude, the amplitudes of the upward-propagating secondary GWs grow exponentially in altitude as $\exp(z/2\mathcal{H})$ (as long as the GWs do not attenuate and the background wind does not change with height). Therefore, the GW amplitudes double every $\Delta z = 2\mathcal{H}\ln 2 = 1.39\mathcal{H}$ in altitude, which is $\Delta z \simeq 9.7$ km for $\mathcal{H} = 7$ km. If an upward-propagating secondary GW is created at $z_i = 50$ km with an amplitude that is 5 times smaller than that of the MW, its amplitude will be approximately equal to that of the MW (before it broke) when this secondary GW reaches $z = z_i + 2\ln(5)\mathcal{H} \simeq 73$ km for these idealized conditions.

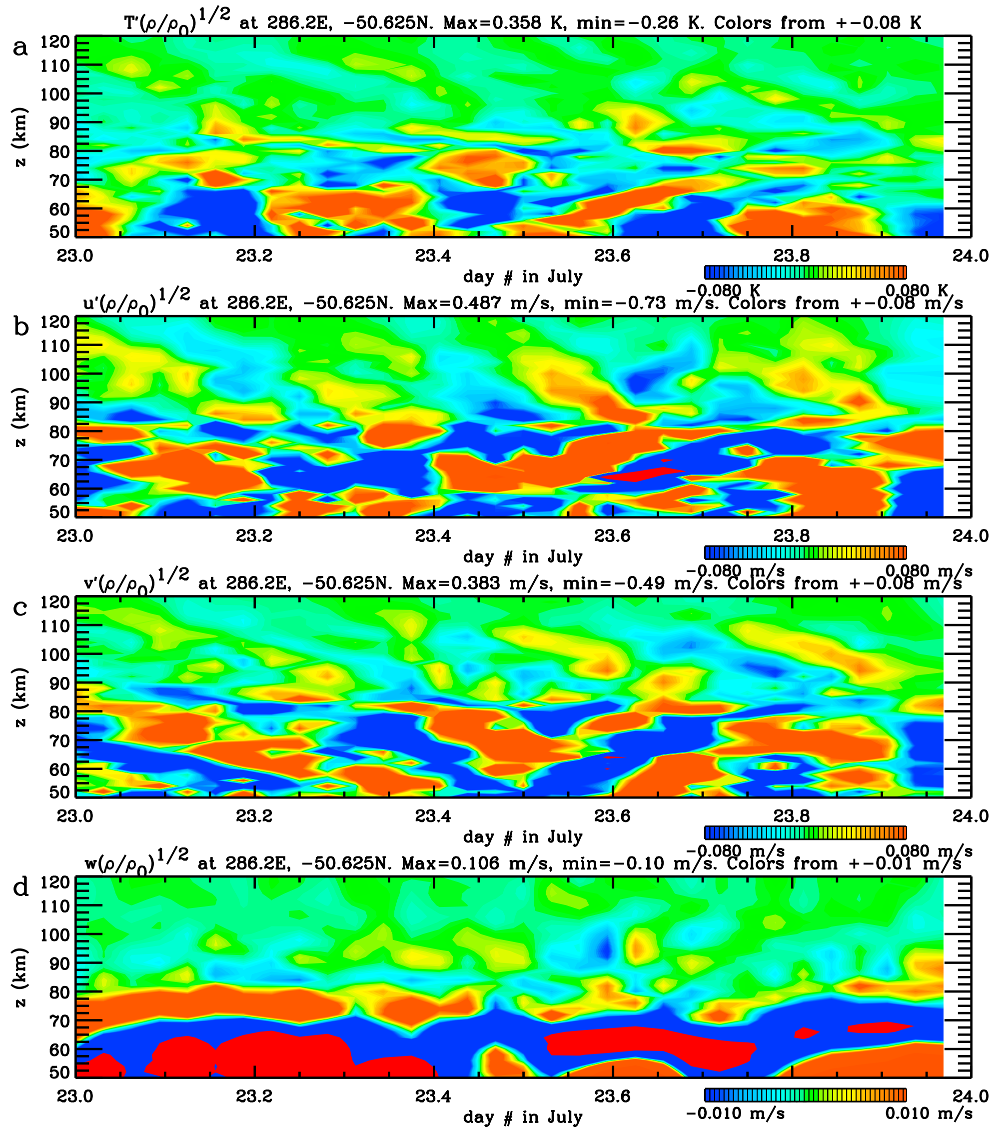

Figure 6. Same as in Figure 5 but at $z = 50$–120 km on 23–24 July. The colors are oversaturated at the lower altitudes to enhance the gravity waves at the higher altitudes.

From Figure 6, we see that the secondary GWs have periods of $\tau_r \sim 4$–11 hr. While some of the secondary GWs with $|\lambda_z| \sim 10$–15 km attenuate at $80 < z < 90$ km, others with $|\lambda_z| \sim 15 - 20$ km propagate above 90 km.

Figure 7 shows transformed horizontal slices of T' on 23.40625 July at $z = 60$ to 90 km. At $z = 60$ and 70 km, small-scale GWs with $\lambda_H \sim 165$–215 km are overlayed on medium-scale GWs with $\lambda_H \sim 215$–375 km at $x'' \sim 0$ to 1,000 km and $y'' \sim -1,500$ to -500 km. This is caused by the breaking of the MWs that were swept downstream, as well as the biproducts of the nonlinear cascade to turbulence that in the model is balanced by the diffusion scheme. Additionally, partial concentric rings of GWs are seen southwest of the Antarctica Peninsula. Because these rings occur at $z = 60$ km, which is in the middle of the MW breaking region, these concentric ring GWs could be upward- or downward-propagating secondary GWs. At $z = 90$ km, we see concentric rings of GWs with estimated centers at $\simeq 300°$ E and $\simeq 60$–$65°$ S (i.e., $x'' \simeq 0$ and $y'' \simeq -1,500$ to $-1,000$ km). The largest-amplitude concentric GWs propagate southwestward and have $\lambda_H \sim 1,000$–$2,000$ km. There are also weaker concentric GWs that propagate northeastward at $z = 90$ km, with $\lambda_H \sim 500$–$1,000$ km. Some of these concentric GWs may also be breaking. Note that there is a small

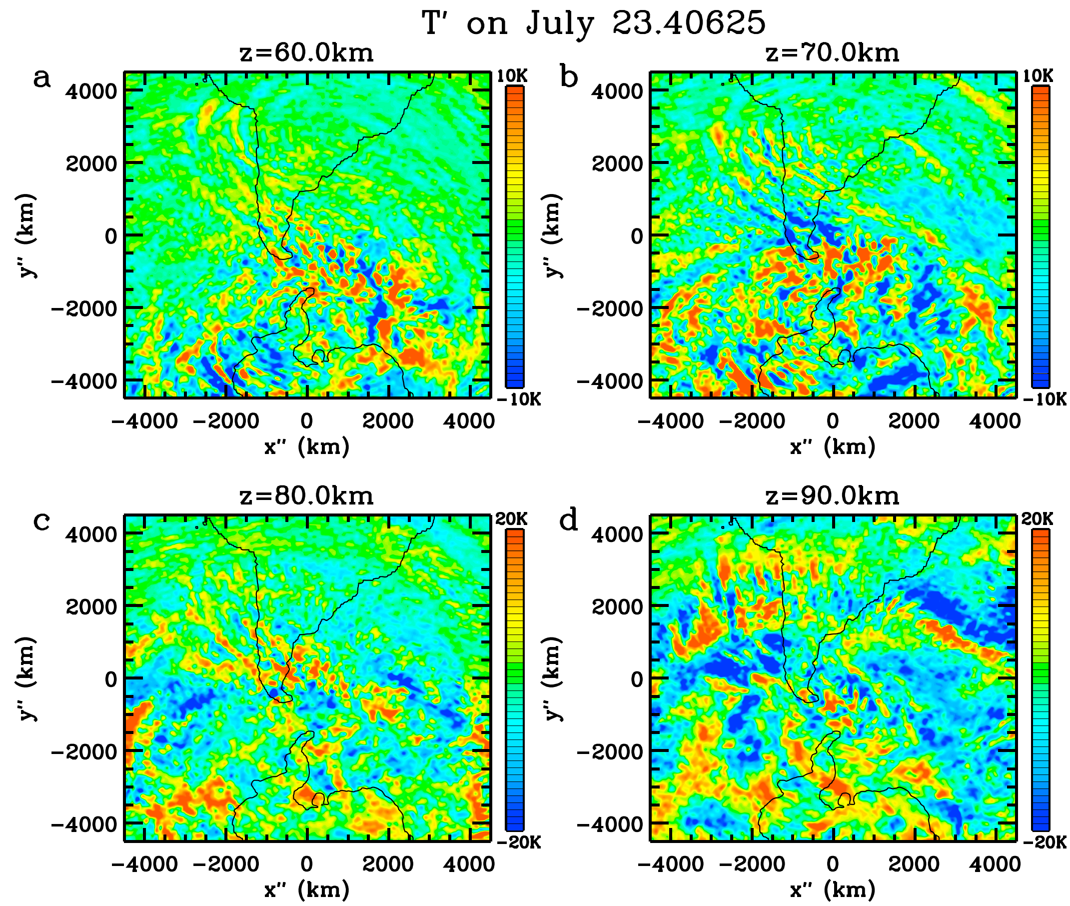

Figure 7. T' (in K) at $z = 60$ km (a), 70 km (b), 80 km (c) and 90 km (d) on 23.40625 July. $x'' = y'' = 0$ is located at 300° E and 50° S.

region where MW breaking still occurs at $z = 80$ km (i.e., at $x'' \simeq -3,000$ to 1,000 km and $y'' \simeq -500$ to 1,500 km); this region is not present at $z = 90$ km.

We now show that the centers of the concentric GWs at $z = 80$ and 90 km in Figures 7c and 7d coincide with the locations of the local body forces created from the breaking and attenuation of the GWs. We compute the convergence of the pseudo momentum flux (Appendix A of VB18)

$$F_x = -\frac{1}{\bar{\rho}}\partial_z\left(\bar{\rho}\left(\overline{u'w'} - \frac{f\,C_p}{g}\overline{T'v'}\right)\right), \quad F_y = -\frac{1}{\bar{\rho}}\partial_z\left(\bar{\rho}\left(\overline{v'w'} + \frac{f\,C_p}{g}\overline{T'u'}\right)\right), \tag{8}$$

where F_x and F_y are the zonal and meridional components of the local body forces. Here primes denote deviations from the background flow, and the overlines denote averages over several GW wavelengths. Additionally, g is the gravitational acceleration, $f = 2\Omega \sin\theta$ is the Coriolis parameter in the f-plane approximation, $\Omega = 2\pi/24$ hr, and θ is a fixed latitude.

Figures 8 and 9 show F_x and F_y, respectively, every 10 km in altitude from $z = 50$ to 160 km on 23.4 July. At $z \sim 50$ to 80 km in Figures 8 and 9, most of the body forces are westward and southward and are located directly over the Southern Andes. These forces are created by the attenuation of MWs that propagate directly upward from the Southern Andes. There are also body forces located southeast of the southern tip of South America at $x'' \sim -500$ to 2,000 km and $y'' \sim -1,500$ to 0 km (i.e., at ∼293–330° E and ∼50–65° S) having very large amplitudes of 900–2200 m/s/day. These forces are caused by the attenuation of the MWs that are swept downstream from the Southern Andes (see Figure 1b) and appear to be located at the approximate centers of the concentric rings in Figures 7c and 7d. Therefore, it is likely that the concentric rings of GWs at $z = 80$ and 90 km in Figures 7c and 7d are secondary GWs generated by the local body forces created by the deposition of momentum from MW breaking. Above the transition altitude at $z \sim 80$ km, most of the body forces are eastward and northward and are located east of the South American continent. These

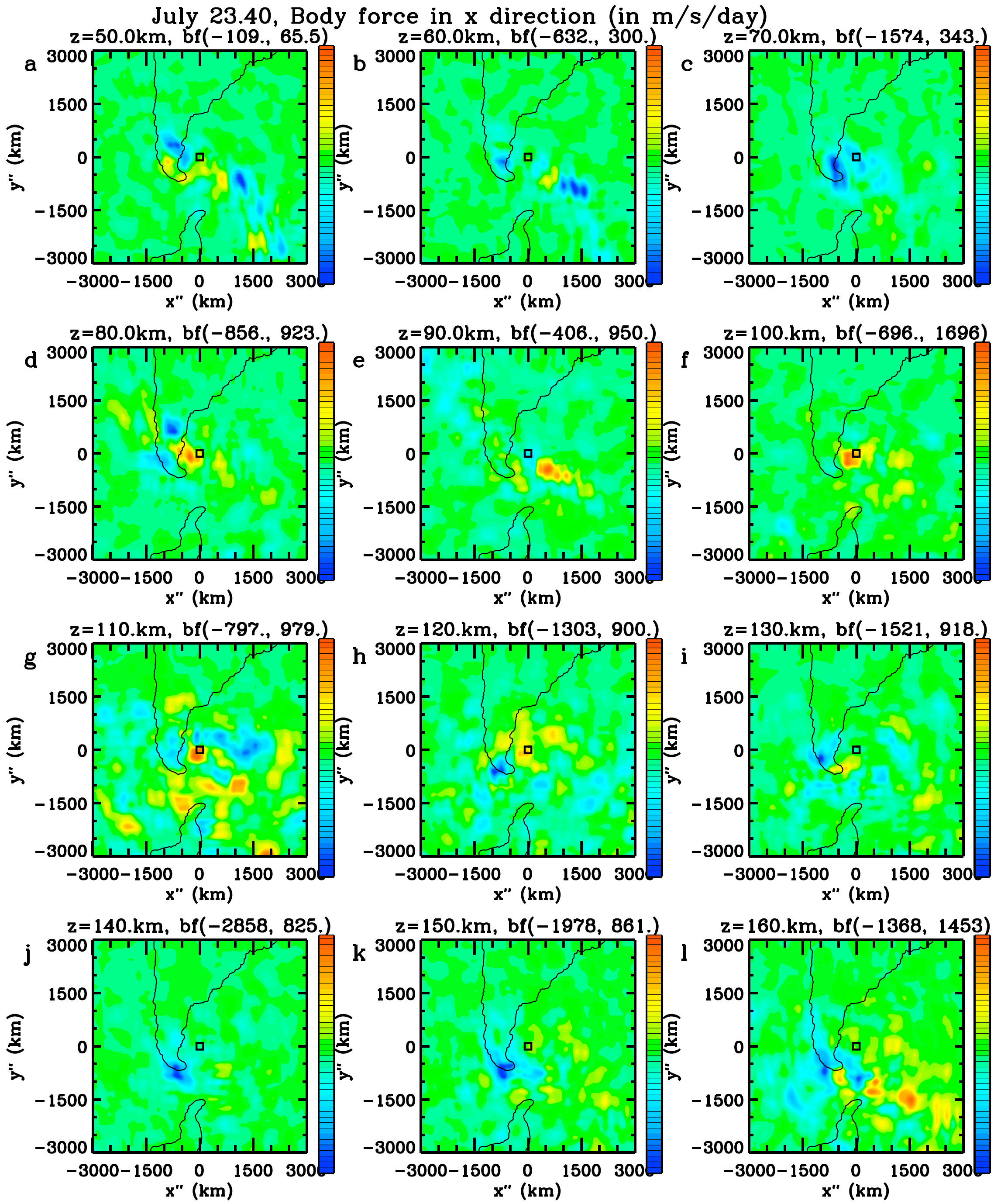

Figure 8. F_x (in m/s/day) every 10 km from z = 50 km to 160 km (a-l, respectively) on 23.4 July. $x'' = y'' = 0$ is located at 300° E and 50° S (denoted by small black squares). Maximum and minimum values of the body force (in m/s/day) are shown at the top of each panel in parentheses. F_x is scaled by the maximum of the absolute value of F_x, denoted by β; the blue to red colors go from $-\beta$ to β, respectively.

forces are caused by the attenuation of northeastward-propagating secondary GWs. Note that there is a large range of horizontal scales in F_x and F_y of 180–800 km. The larger scales are created by the attenuation of the MW packets, while the smaller scales are created by the constructive and destructive interference between attenuating MWs that arrive from different parts of the Southern Andes.

A general trend from Figure 5 is that the secondary GW amplitudes are small (large) in the mesosphere during weak (strong) MW events. For example, the secondary GW amplitudes at $z \sim$ 60–80 km are small

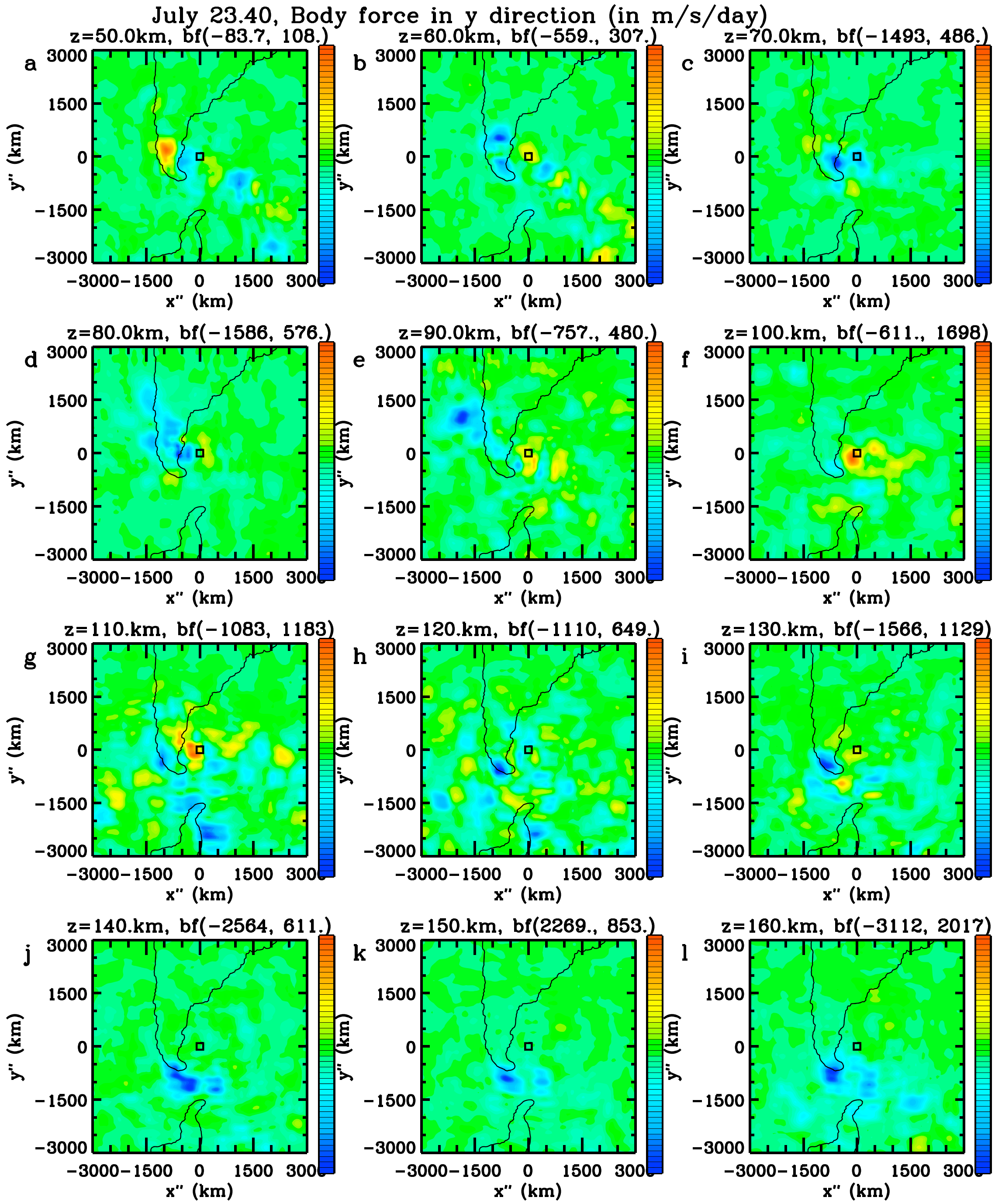

Figure 9. Same as in Figure 8 but for F_y.

on 19.0–20.0 July and are large on 20.0–21.0 July, even though (1) the initial MW amplitudes at $z = 5$ km are similar on 19.0 and 20.0 July (see Figure 5d) and (2) secondary GWs are generated at $z \sim 20$–30 km on 19.25–19.75 July from MW breaking (see the fishbone structures in Figure 5c). Why do these latter secondary GWs (generated at lower altitudes during weak MW events) not also have large amplitudes in the mesosphere? This is partly because these GWs are filtered by the stratospheric jet, since their propagation directions have significant zonal components. But even if this was not the case, it turns out that a secondary GW's amplitude at a given altitude z is exponentially larger when the body force that generates it is located higher in altitude, as we show now.

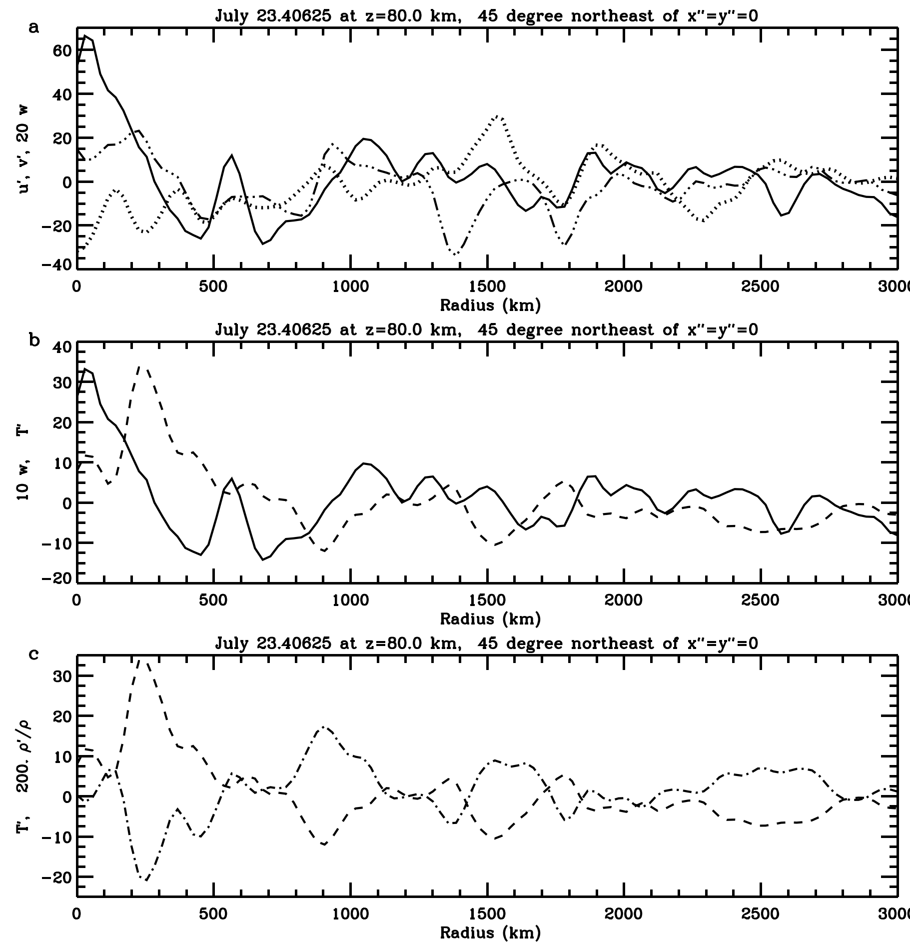

Figure 10. The result on 23.4062 July at $z = 80$ km on a line 45° northeast from 300° E and 50° S. (a) u' (in m/s, dot line), v' (in m/s, dash-dot-dot-dot line), and $20w$ (in m/s, solid line). (b) $10w$ (in m/s, solid line) and T' (in K, dash line). (c) T' (in K, dash line) and $200\rho'/\bar{\rho}$ (dash-dot line).

Let us assume that a primary GW is excited at z_i and then attenuates and creates a body force at z_b. At $z = z_b$, this GW's amplitude is $\propto e^{(z_b-z_i)/2\mathcal{H}}$. The amplitude of the body force it creates is proportional to the primary GW amplitude squared from equation (8). Additionally, the initial secondary GW amplitudes are proportional to the body force amplitude (Vadas et al., 2003). Therefore at a given altitude z whereby $z > z_b$, the amplitude of an excited secondary GW is proportional to

$$\propto [e^{(z_b-z_i)/2\mathcal{H}}]^2 e^{(z-z_b)/2\mathcal{H}} = e^{(z+z_b-2z_i)/2\mathcal{H}} = e^{(z-z_i)/2\mathcal{H}} e^{(z_b-z_i)/2\mathcal{H}}. \tag{9}$$

Equation (9) shows that the amplitude of a secondary GW at a given height z depends sensitively and exponentially, as $e^{z_b/2\mathcal{H}}$, on the body force altitude. This is because the secondary GW amplitude is proportional to the primary GW amplitude squared. If the primary GW propagates higher (lower) before attenuating, then the amplitudes of the secondary GWs at a given z will be larger (smaller). Thus, the secondary GW amplitudes at a fixed z depend not only on the initial MW amplitudes but also on the properties of the stratospheric jet. This is the main reason why the secondary GW amplitudes in the mesosphere are larger (smaller) during strong (weak) MW events in Figure 5.

Figure 10 shows u', v', w, T', and $\rho'/\bar{\rho}$ along a line 45° northeast from 300° E and 50° S (i.e., starting at $x'' = y'' = 0$) in the (x'', y'') 2-D plane at $z = 80$ km on 23.4062 July (see Figure 7c for T'). GWs and wave motions are visible with $\lambda_H \sim$ 200–1,000 km, $T' \sim$ 2–10 K, and $\rho'/\bar{\rho} \sim$ 1–8%. Although w' and T' are often 90° out of phase and T' and ρ' are often 180° out of phase, this is not always the case; such effects can occur if a GW has $|\lambda_z| >\sim \pi\mathcal{H}$ (Vadas, 2013) or if it is attenuating (Vadas & Nicolls, 2012).

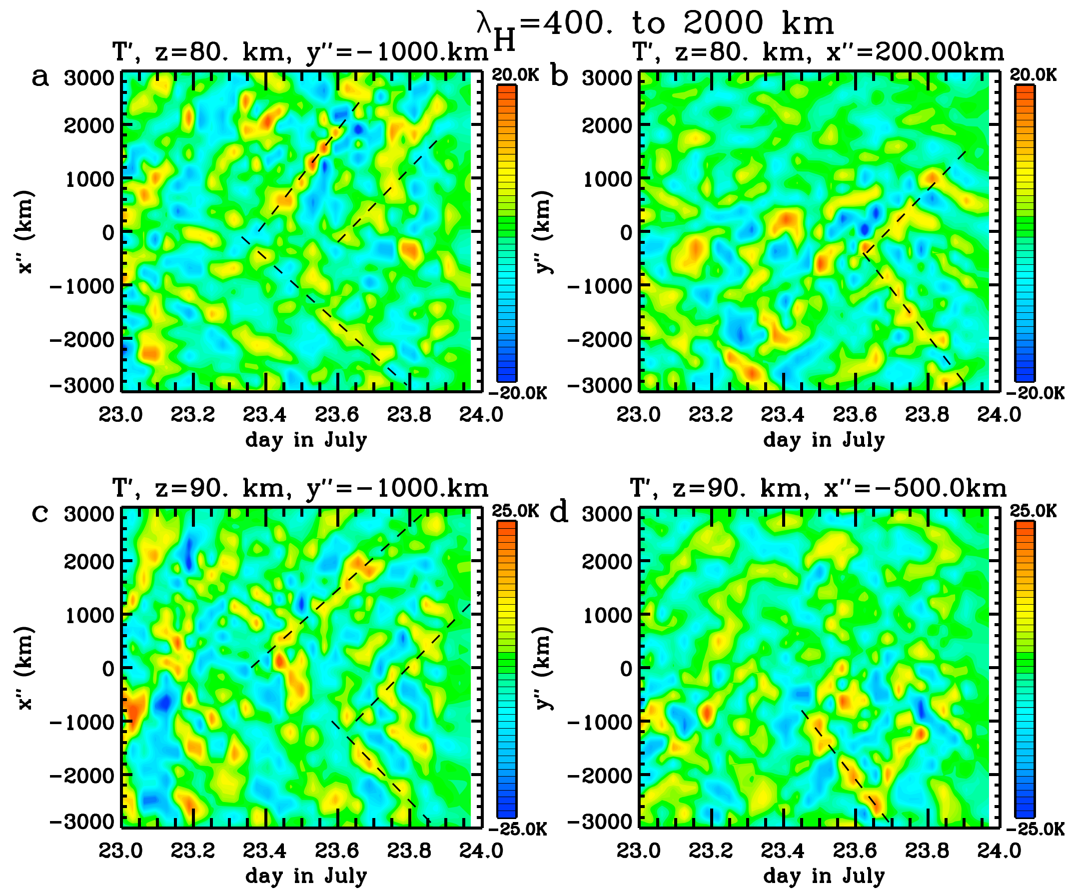

Figure 11. Keograms of T' for gravity waves with $400 < \lambda_H < 2,000$ km on 23 July. (a) $y'' = -1,000$ km at $z = 80$ km. The dashed lines show $c_x = 100$, 80, and -70 m/s. (b) $x'' = 200$ km at $z = 80$ km. The dashed lines show $c_y = 80$ and -100 m/s. (c) $y'' = -1,000$ km at $z = 90$ km. The dashed lines show $c_x = 70$ and ± 80 m/s. (d) $x'' = -500$ km at $z = 90$ km. The dashed line shows $c_y = -100$ m/s. $x'' = y'' = 0$ is located at 300° E and 50° S.

We showed in Figures 7c and 7d that the secondary (concentric) GWs had $\lambda_H \simeq 700$–2,000 km during the 23 July event. We now determine their horizontal phase speeds. We create transformed 2-D horizontal slices of $T'\sqrt{\bar{\rho}/\bar{\rho}_0}$ at $z = 80$ and 90 km (similar to Figure 7 but only for $-3,000 \le x'' \le 3,000$ km and $-3,000 \le y'' \le 3,000$ km), apply 2-D Fourier transforms, extract those GWs with $400 < \lambda_H < 2,000$ km, and then apply the inverse Fourier transforms. This allows for the isolation of GWs having the desired horizontal wave scales. Figures 11a and 11c show "keograms" of T' for these GWs at $z = 80$ and 90 km, respectively, as functions of x'' and time at $y'' = -1,000$ km. (This location is close to the centers of the concentric rings in Figures 7c and 7d.) The largest-amplitude eastward- and westward-propagating GWs have horizontal phase speeds of $c_H \sim 70$–100 m/s. Figures 11b and 11d show keograms of T' at $z = 80$ and 90 km, respectively, as functions of y'' and time at $x'' = 200$ and -500 km, respectively. The largest-amplitude northward- and southward-propagating GWs have similar horizontal phase speeds of $c_H \sim 80$–100 m/s. Note that these GWs have $\lambda_H \sim 500$–2,000 km (in agreement with Figure 7) and $\tau_r \sim 3$–10 hr.

We now investigate what happens to the secondary GWs at $z > 90$ km. Figure 12 shows $T'\sqrt{\bar{\rho}/\bar{\rho}_0}$ at 299.7° E and 49.8° S at $z = 80$–130 km on 23 July for GWs with $400 < \lambda_H < 2,000$ km. This location is ~1,000 km farther east than in Figure 6a. Here we create transformed 2-D horizontal slices of $T'\sqrt{\bar{\rho}/\bar{\rho}_0}$ for each z (as in Figure 7), apply 2-D Fourier transforms, extract those GWs with the desired values of λ_H, and then apply the inverse Fourier transforms. In Figure 12, there is a decrease in the GW amplitudes at $z \sim 90$ to 100 km due to the dissipation of many of the secondary GWs (BV18). However, there is a significant increase in the GW amplitudes and in $|\lambda_z|$ at $z = 110$ to 130 km (e.g., many of the phase lines are nearly vertical). Setting

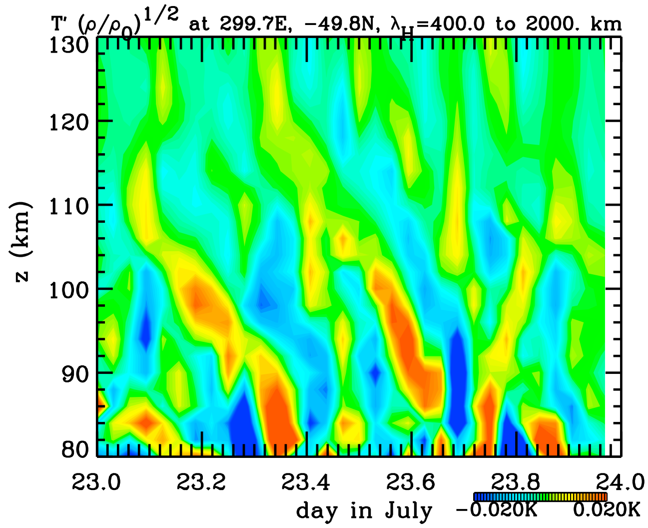

Figure 12. $T'\sqrt{\bar{\rho}/\bar{\rho}_0}$ at 299.7° E and 49.8° S at $z = 80$–130 km on 23–24 July for gravity waves with $400 < \lambda_H < 2,000$ km. Here $\bar{\rho}_0 = 878.877\ \mathrm{g/m^3}$ is the value of $\bar{\rho}$ at 0° E, 89.625° S and $z = 4$ km on 23.0 July.

the GW phase, $mz - \omega_r t$, constant, we estimate $|\lambda_z|$ as

$$|\lambda_z| = \frac{\Delta z}{\Delta t}\tau_r, \tag{10}$$

where $\Delta z/\Delta t$ is the slope of the phase line in a $z - t$ plot at a fixed x and y. Using $\tau_r \simeq 5$ hr at $z \simeq 120$–130 km on 23.3 July in Figure 12, we estimate $|\lambda_z| \simeq 130$ km. As we show in section 4.4, these GWs are tertiary GWs generated from the local body forces created by the attenuation of secondary GWs. Note that the phase lines are upward in time at $z = 90$–110 km on 23.8 July, thereby suggesting that downward-propagating tertiary GWs are created at $z \simeq 110$ km at that time.

4.4. Excitation of Tertiary GWs

We now focus on the simulated attenuation of secondary GWs, the creation of local body forces, and the excitation of tertiary GWs during the strong orographic event on 23 July. Figure 13 shows the density-scaled quantities at 286.2° E, 50.625° S, and $z = 80$–170 km on 23 July. The secondary GWs dissipate at $z \sim 90$–130 km. Above this altitude, smaller-amplitude GWs with $\tau_r \sim 2$–11 hr and much larger $|\lambda_z|$ appear. Note that T', u', and v' emphasize the longer-period, smaller-$|\lambda_z|$ GWs, while w emphasizes the shorter-period, larger-$|\lambda_z|$ GWs. (GWs with periods of ~2 hr are easily seen in Figure 13d.) This model result demonstrates that these GWs are not monochromatic GWs, because if they were, T', u', v', and w would show the same waves. Instead, there is a broad spectrum of GWs. At $z \geq 110$ km, the GWs generally have downward phases in time. However, the phases are upward in time on 23.0–23.2 July at $z \sim 110$–150 km in Figure 13d, thereby suggesting that downward-propagating GWs are created at $z \simeq 150$ km at that time. These downward-propagating GWs could either be (1) tertiary GWs created from the attenuation of secondary GWs at $z \sim 150$ km or (2) higher-order GWs created from the attenuation of tertiary GWs at $z \sim 150$ km.

Figure 14 shows transformed horizontal slices of T' on 23.4375 July at $z = 100$ to 160 km. Concentric rings of GWs are seen, with centers at $x'' \sim 0$ and $y'' \sim 0$ (i.e., at ~300° E and ~50° S). These GWs have $\lambda_H \sim 350$–1,500 km, with λ_H increasing significantly with radius from the ring centers. For example, at $z = 140$–160 km, those GWs near the centers have $\lambda_H \sim 350$ km, while those over the South Atlantic Ocean at large radii (i.e., at $x'' = 1,000$–3,000 km and $y'' = 0$–3,000 km) have $\lambda_H \sim 1,000$–1,500 km.

From Figures 8 and 9, there is a very strong northeastward body force at ~300° E and ~50° S at $z = 80$–130 km. This force maximizes at $z \simeq 110$ km with a large amplitude of ≃2,400 m/s/day. Because this body force is ~600–1,000 km east of the Southern Andes, is many tens of kilometers above the altitude range where the MWs break, and is located in the altitudinal range where the secondary GWs dissipate (see Figures 12 and 13), we infer that this body force is created by the dissipation of secondary GWs. Importantly, this body force is located at the approximate center for most of the concentric rings of GWs in Figure 14.

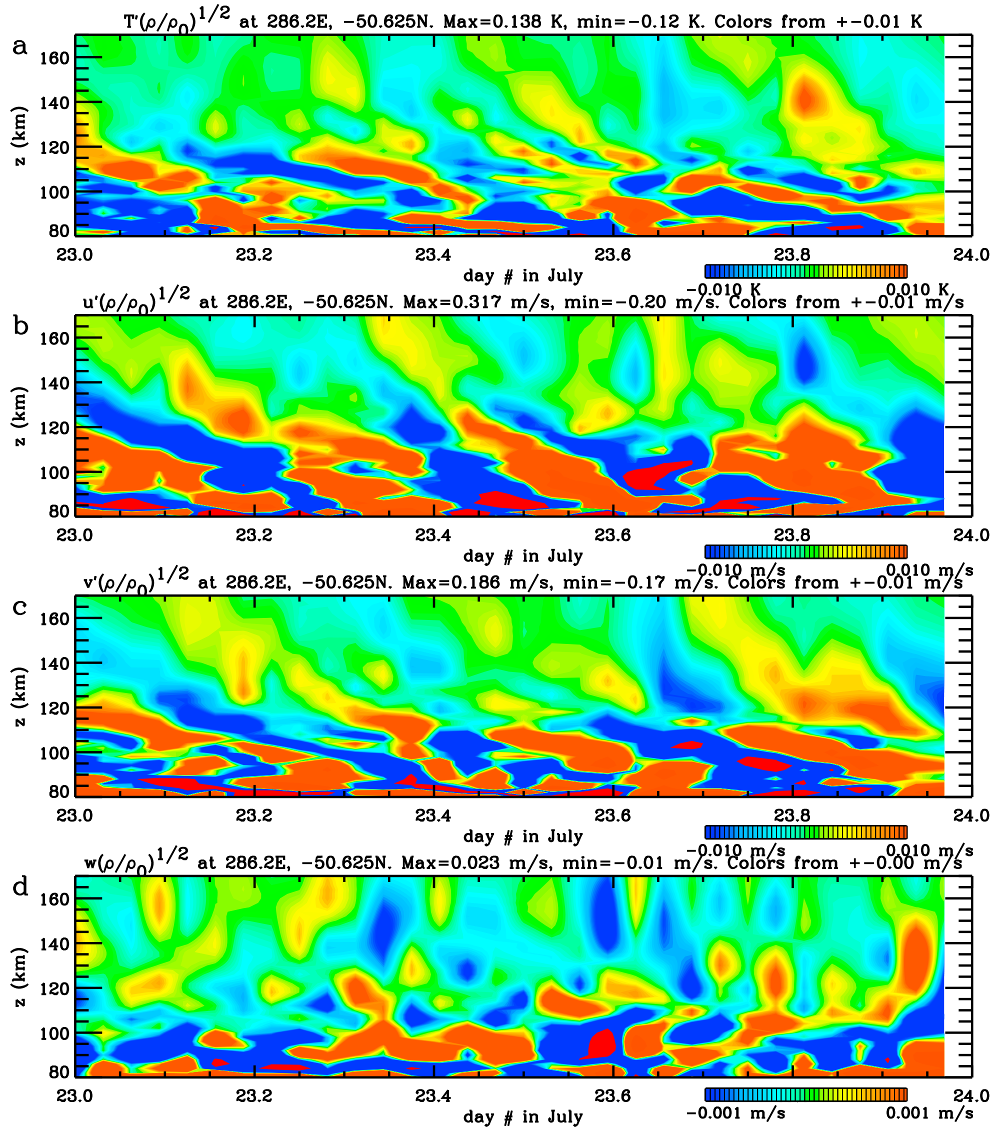

Figure 13. Same as in Figure 6 but at z = 80–170 km.

Therefore, the concentric rings of GWs at z = 100–160 km in Figure 14 are mainly tertiary GWs generated by the local body forces created by the deposition of momentum from the attenuation of secondary GWs.

The spectrum of GWs generated by a body force is broad, with a wide range of horizontal and vertical wavelengths and periods (Vadas et al., 2003). The GW polarization relations cause different parts of a *broad* GW spectrum to be emphasized, depending on which quantity is measured. For example, the polarization relation relating w' and T' for a midfrequency GW with $|\lambda_z| < 2\pi\mathcal{H}$ is

$$w' = -\frac{ig\omega_{Ir}}{\bar{T}N_B^2}T' \tag{11}$$

(Equation (44) of Vadas et al., 2018). This causes the amplitude of w' to be relatively large (as compared to the amplitude of T') for GWs with large intrinsic frequencies. The result is that the spectrum of GWs excited by a body force peaks at larger horizontal wavelengths, smaller vertical wavelengths, and larger periods in measurements of T', u', and v' than in measurements of w' (Figure 4 of Vadas et al., 2018). On a horizontal plane at a given altitude and time above a body force, the GWs excited by this force have widely varying wavelengths and periods; in particular, those GWs having larger radii from the ring center have larger λ_H, $|\lambda_z|$, and τ_{Ir}, with λ_H increasing as the radius squared (Equations (48)–(52) of Vadas et al., 2018). The GW

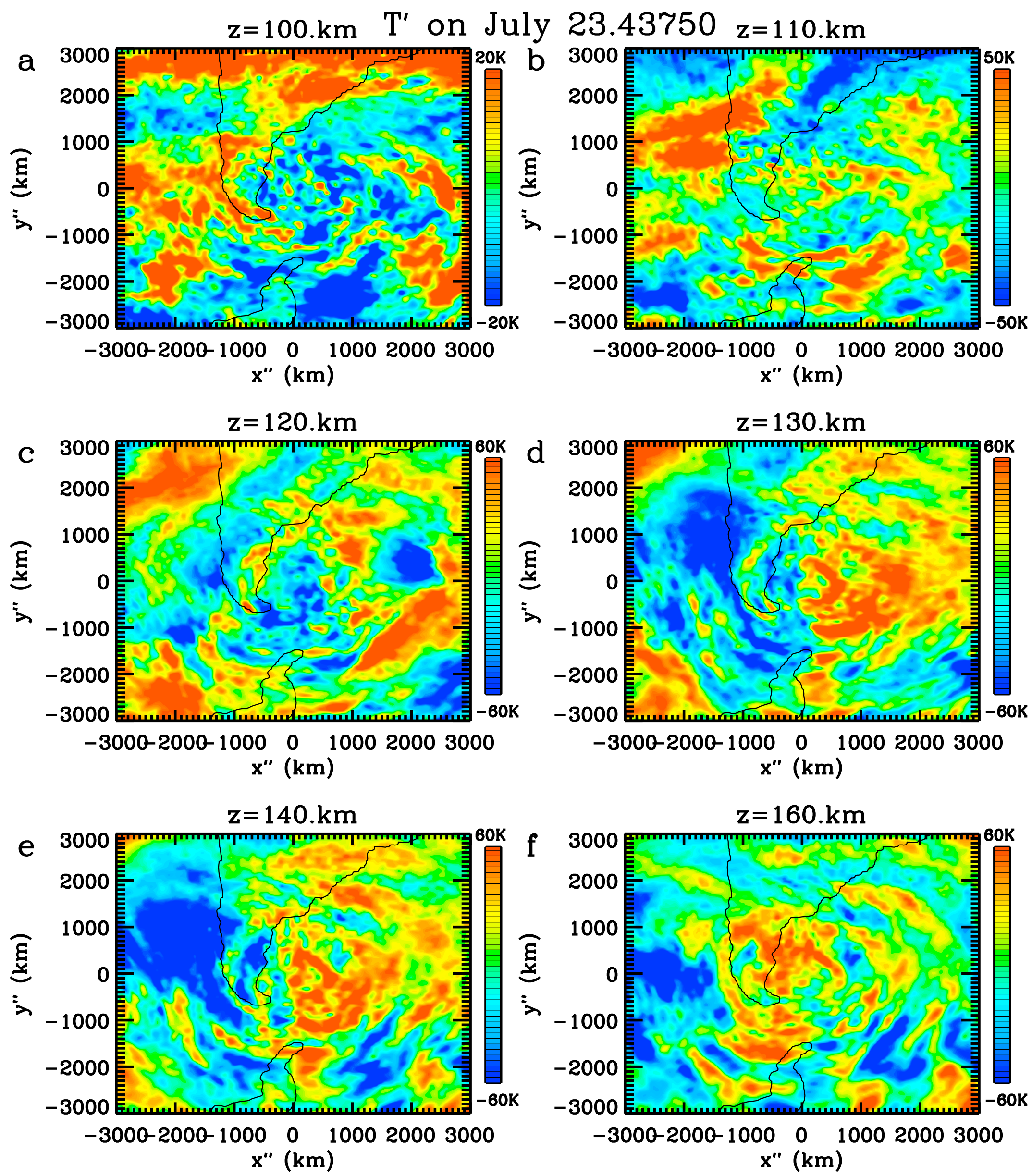

Figure 14. T' at z = 100 km (a), 110 km (b), 120 km (c), 130 km (d), 140 km (e) and 160 km (f) on 23.4375 July. $x'' = y'' = 0$ is located at 300° E and 50° S.

polarization relations again cause those GWs with larger τ_{Ir} to have larger amplitudes in T', u', and v', while those GWs with smaller τ_{Ir} have larger amplitudes in w'. This explains why the shorter-period tertiary GWs (which typically have larger $|\lambda_z|$) are easily seen in w, while the longer-period tertiary GWs (which typically have smaller $|\lambda_z|$) are easily seen in T', u', and v' in Figure 13 at $z \geq 110$ km.

According to theory, (1) the tertiary GWs propagating exactly in and against the force direction have the largest amplitudes, and (2) tertiary GWs propagate in all directions except those perpendicular to the force direction (Vadas et al., 2003). Because the force located at z = 80–130 km, $x'' \sim 0$ and $y'' \sim 0$ (i.e., at 300° E and 50° S) is northeastward in Figures 8 and 9, we infer that the generated tertiary GWs from this body force will propagate in all directions except northwestward and southeastward; this is seen to be the case in Figure 14f at z = 160 km for the largest-amplitude concentric GWs having large radii from the ring center. Indeed, at radii > 1,000 km, those concentric GWs having the largest amplitudes propagate mainly northeastward (i.e., located at $x'' \sim$ 500 to 2,500 km and $y'' \sim$ 0 to 2,000 km) and southwestward (i.e., located at

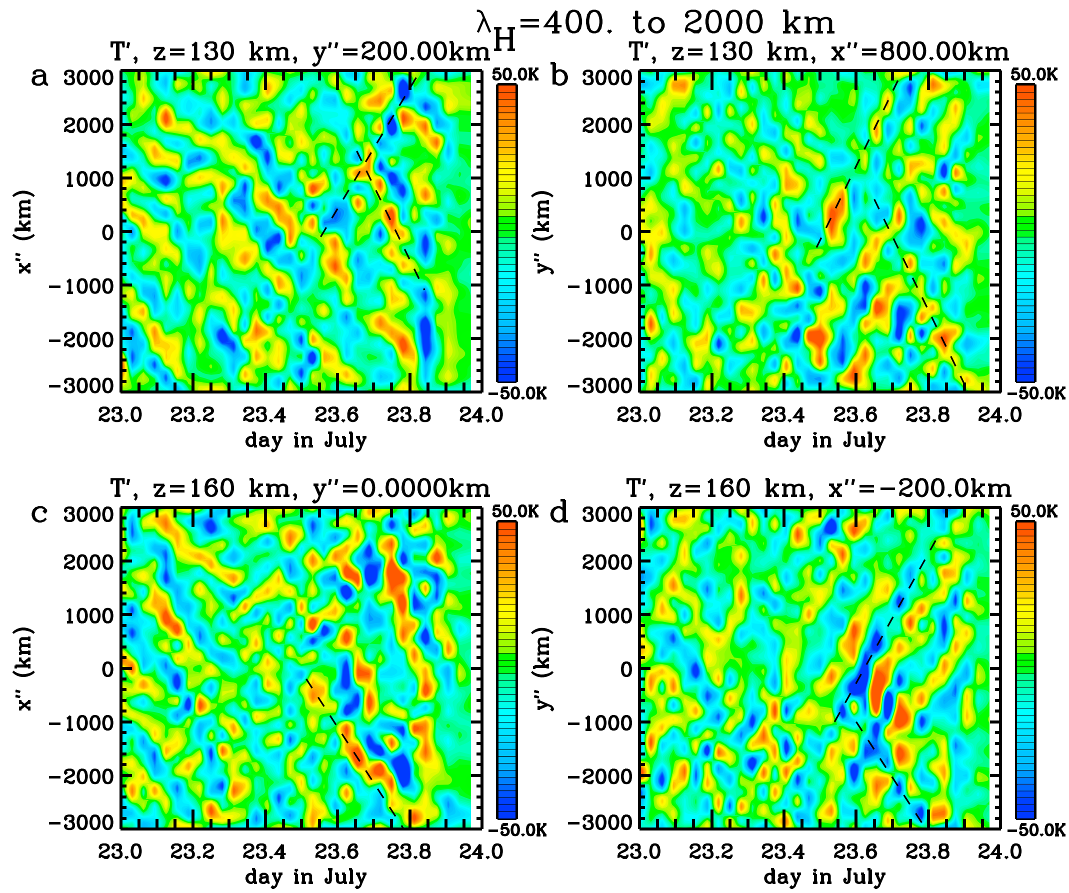

Figure 15. Keograms of T' for gravity waves with $400 < \lambda_H < 2,000$ km on 23 July. (a) $y'' = 200$ km at $z = 130$ km. The dash lines show $c_x = 130$ and -160 m/s. (b) $x'' = 800$ km at $z = 130$ km. The dash lines show $c_y = \pm 160$ m/s. (c) $y'' = 0$ at $z = 160$ km. The dash line shows $c_x = -120$ m/s. (d) $x'' = -200$ km at $z = 160$ km. The dash lines show $c_y = 140$ and -120 m/s. $x'' = y'' = 0$ is located at 300° E and 50° S.

$x'' \sim -2,000$ to 0 km and $y'' \sim -3,000$ to -500 km). The likely reason that there are smaller-amplitude concentric GWs propagating northwestward and especially southeastward in Figure 14f is because tertiary GWs are also excited from other (smaller-amplitude) body forces. For example, the weaker westward body force near the southern tip of South America at $z \sim 120$ km in Figures 8 and 9 would excite smaller-amplitude concentric GWs, some of which would propagate northwestward and southeastward. As we show below, those upward-propagating tertiary GWs having a significant westward component are attenuated partially/fully by critical level filtering and molecular viscosity; this is likely why the northwestward GWs have much smaller amplitudes than the southeastward GWs at radii $> 1,000$ km in Figure 14f.

From Figure 14, the tertiary GWs have $\lambda_H \sim 350$–1,500 km during the July 23 event. We now determine their horizontal phase speeds. Figures 15a and 15c show keograms of T' as functions of x'' and time at $z = 130$ and 160 km, respectively, at $y'' = 200$ and 0 km, respectively, for GWs with $400 < \lambda_H < 2{,}000$ km. The largest-amplitude GWs propagating eastward and westward have $c_H \simeq 130$–160 m/s. Figures 15b and 15d show keograms of T' as functions of y'' and time at $z = 130$ and 160 km, respectively, at $x'' = 800$ and -200 km, respectively. The largest-amplitude GWs propagating northward and southward have similar values: $c_H \simeq 120$–160 m/s. They also have $\lambda_H \sim 1{,}000$–2,000 km (in agreement with Figure 14) and $\tau_r \sim 4$–9 hr. Note that these large-scale tertiary GWs are inertia GWs with large vertical wavelengths.

From Figures 14d and 14e, the tertiary GWs propagating southwestward near the southern tip of South America have much smaller amplitudes than those propagating northeastward. This indicates that the southwestward-propagating tertiary GWs are partially attenuated at $z \simeq 140$ km. This is seen to be the case from Figures 8j and 9j, which shows strong southwestward body forces near the tip of South America.

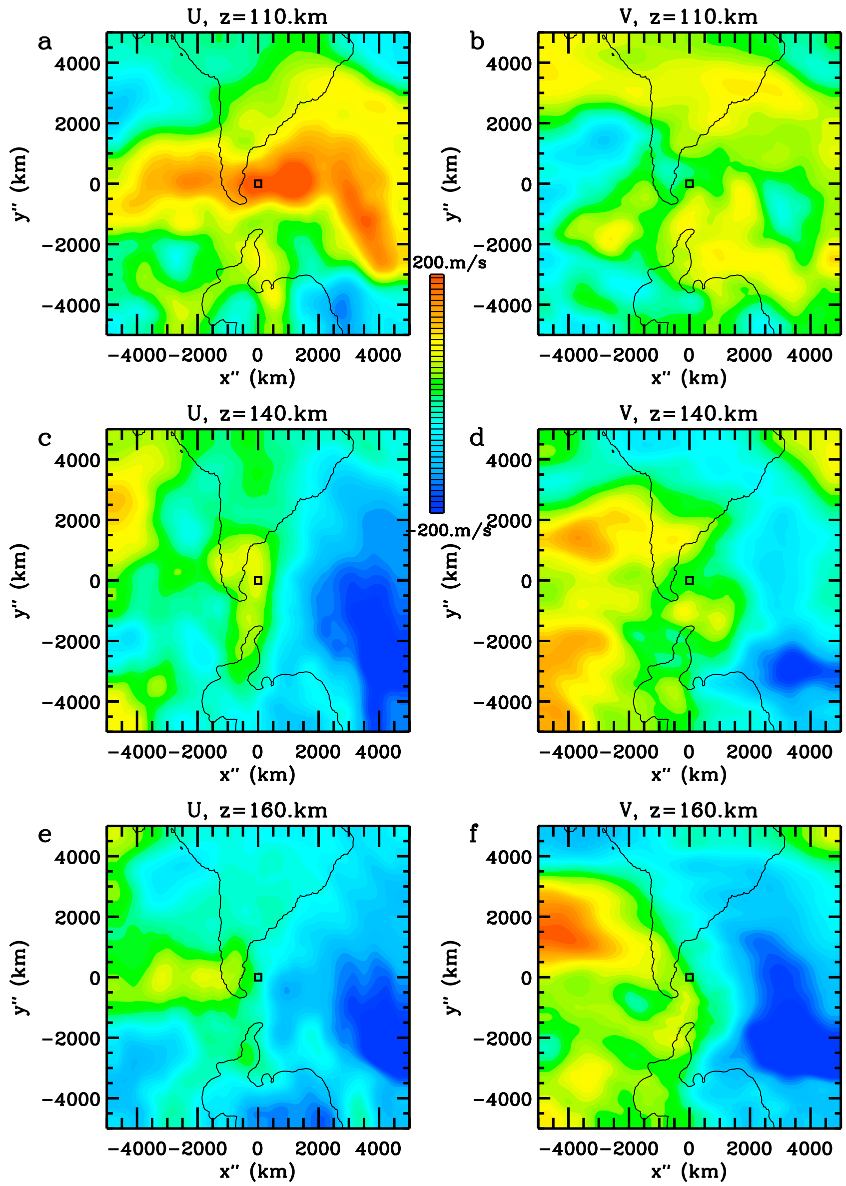

Figure 16. The background wind $\bar{U}$ (a) and $\bar{V}$ (b) at $z = 110$ km on 23.40 July. (c,d) Same as (a) and (b) but for $z = 140$ km. (e,f) Same as (a) and (b) but for $z = 160$ km. $x'' = y'' = 0$ is located at 300° E and 50° S.

Because theory predicts that the initial amplitudes of the northeastward and southwestward tertiary GWs are the same, we therefore infer that the difference in the background wind between $z \sim 140$ km and the excitation altitude must be southwestward. Figure 16 shows $\bar{U}$ and $\bar{V}$ at $z = 110$, 140, and 160 km on 23.40 July. Where the tertiary GWs are excited (i.e., at $z \sim 110$ km and $x'' = y'' = 0$), the wind is strongly eastward, with $\bar{U} \simeq 150$ m/s and $\bar{V} \simeq 0$. At $z = 140$ km, however, the wind is only weakly eastward (or is westward) 1,000–3,000 km southwest of $x'' = y'' = 0$. Thus, those upward-propagating tertiary GWs having a significant westward component to their propagation direction will have $|\lambda_z|$ decrease significantly. These GWs will either reach critical levels or will partially attenuate from molecular viscosity (Vadas, 2007). For those tertiary GWs propagating southwestward, the background wind increases by $\simeq 150/\sqrt{2} = 105$ m/s in the southwest direction. Therefore, southwestward-propagating tertiary GWs with $c_{IH} < 105$ m/s will reach critical levels and attenuate. Those southwestward-propagating tertiary GWs with $c_{IH} > 105$ m/s will have $|\lambda_z|$ decrease significantly and will therefore attenuate significantly from molecular viscosity. This is why the southwestward-propagating tertiary GWs are attenuated in Figures 14d and 14e. The tertiary GWs propagating northeastward, however, have large amplitudes at $z \sim 160$ km (see Figure 14). This is because the

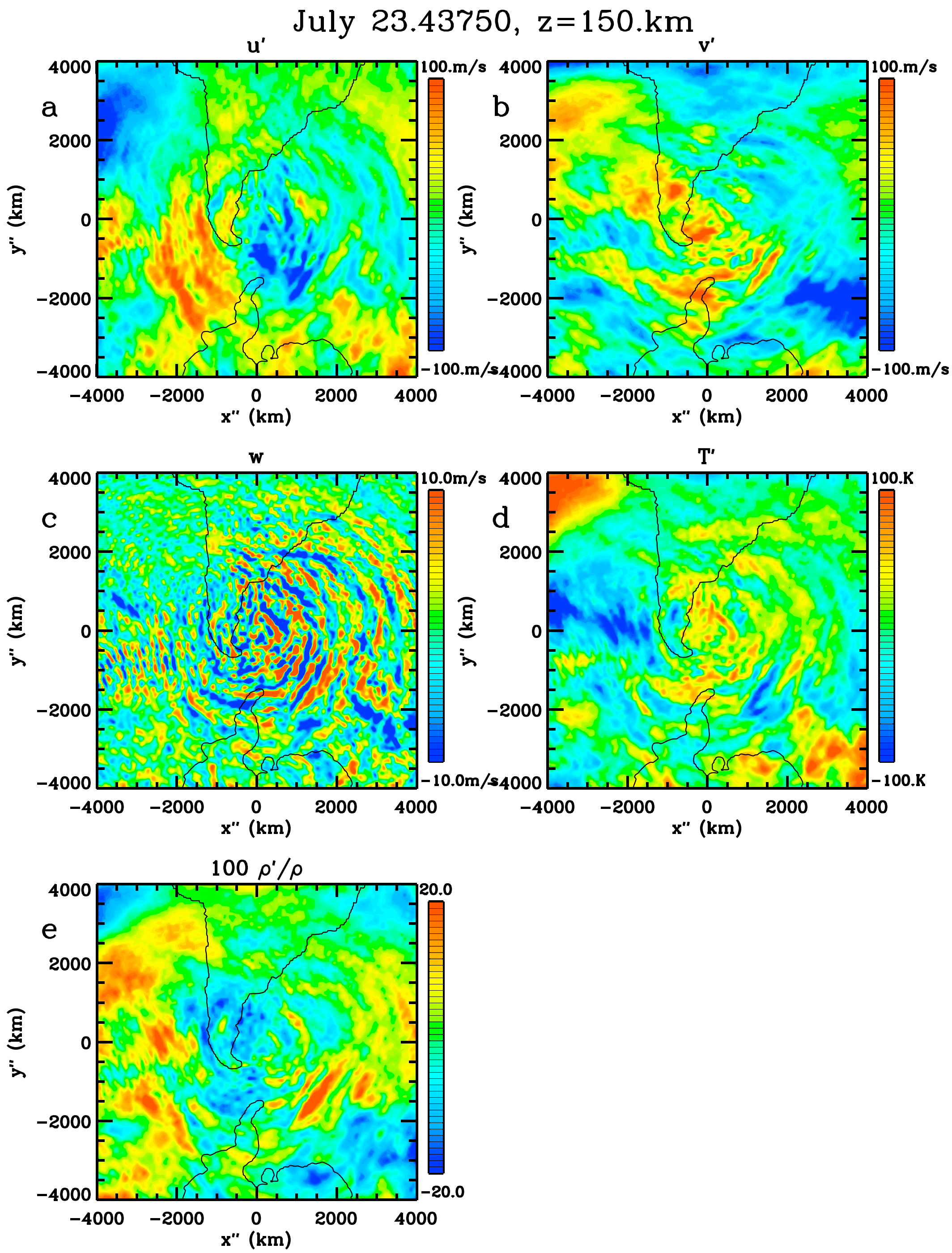

Figure 17. u' (a), v' (b), w (c), T' (d), and $100\rho'/\bar{\rho}$ (e) at $z = 150$ km on 23.4375 July. $x'' = y'' = 0$ is located at 300° E and 50° S.

background wind at $z = 160$ km at $x'' = 0$ to 1,000 km and $y'' = 0$ to 4,000 km is strongly southwestward with $\bar{U} \sim -50$ m/s and $\bar{V} \sim -50$ m/s. Thus, for the tertiary GWs propagating northeastward, the background wind component in the horizontal direction of GW propagation decreases by $\simeq 105 - (-70) \simeq 175$ m/s. This causes $|\lambda_z|$ and c_{IH} to increase significantly for these GWs, thereby enabling them to propagate easily to $z = 160$ km.

Figure 17 shows transformed horizontal slices of u', v', w, T', and $100\rho'/\bar{\rho}$ at $z = 150$ km on 23.4375 July. We see that the concentric ring structures also occur in the horizonal wind and density perturbations, with

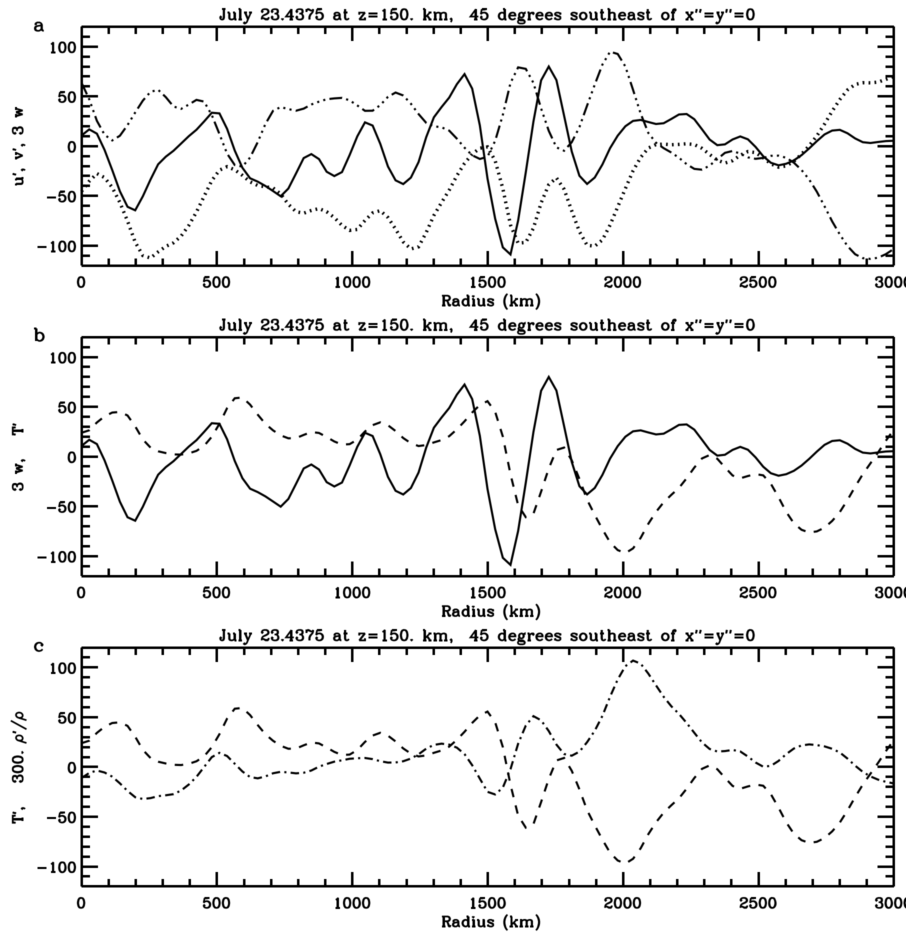

Figure 18. The result on 23.4375 July at $z = 150$ km on a line 45° southeast from 300° E and 50° S. (a) u' (in m/s, dot line), v' (in m/s, dash-dot-dot-dot line), and $3w$ (in m/s, solid line). (b) $3w$ (in m/s, solid line) and T' (in K, dash line). (c) T' (in K, dash line) and $300\rho'/\bar{\rho}$ (dash-dot line).

λ_H increasing significantly with radius from the center of the rings. Because the tertiary GW spectrum is broad, w emphasizes the medium-scale GWs, while T', u', and v' emphasize the larger-scale GWs. The GWs within these ring structures have $u' \sim v' \sim$ 25–50 m/s, $w' \sim$ 1–10 m/s, $T' \sim$ 15–25 K, and $\rho'/\bar{\rho} \sim$ 2–10%. Figure 18 shows u', v', w, T', and $\rho'/\bar{\rho}$ at $z = 150$ km on a line 45° southeast from 300° E and 50° S (i.e., starting at $x'' = y'' = 0$) in the (x'', y'') 2-D plane. The GWs have $\lambda_H \sim$ 200–1,500 km, with $T' \sim$ 10–50 K and $\rho'/\bar{\rho} \sim$ 4–20%. Although ρ' and T' are often 180° out of phase and w' and T' are often 90° out of phase, this is not always the case, especially at smaller radii (i.e., for high frequency GWs).

Figure 19a shows T' on 23.4375 July at $z = 160$ km on a line 45° northeast from 300° E and 50° S (i.e., starting at $x'' = y'' = 0$) in the (x'', y'') 2-D plane. We see that λ_H of the larger-scale GWs increases significantly with radius. This is the expected behavior for GWs excited by a "point source" (such as a local body force), which generates a broad spectrum of GWs. Setting the GW vertical phase speed to be equal at a given time and altitude, the radial dependence of λ_H for GWs generated by a point source is (Equation (52) of Vadas et al., 2018)

$$\lambda_H \simeq |c_z|\tau_B \left[\left(\frac{\mathcal{R}}{\Delta z} \right)^2 + 1 \right], \tag{12}$$

where $\mathcal{R}$ is the radius, $c_z = \omega_{Ir}/m = \lambda_z/\tau_{Ir}$ is the vertical phase speed, and Δz is the vertical distance from the altitude of the force center to the altitude of interest. Therefore, λ_H increases as the radius squared when $\mathcal{R} > \Delta z$. In Figure 19a, we overplot

$$T'_{\rm ps} = A \sin(k_H \mathcal{R} + \phi), \tag{13}$$

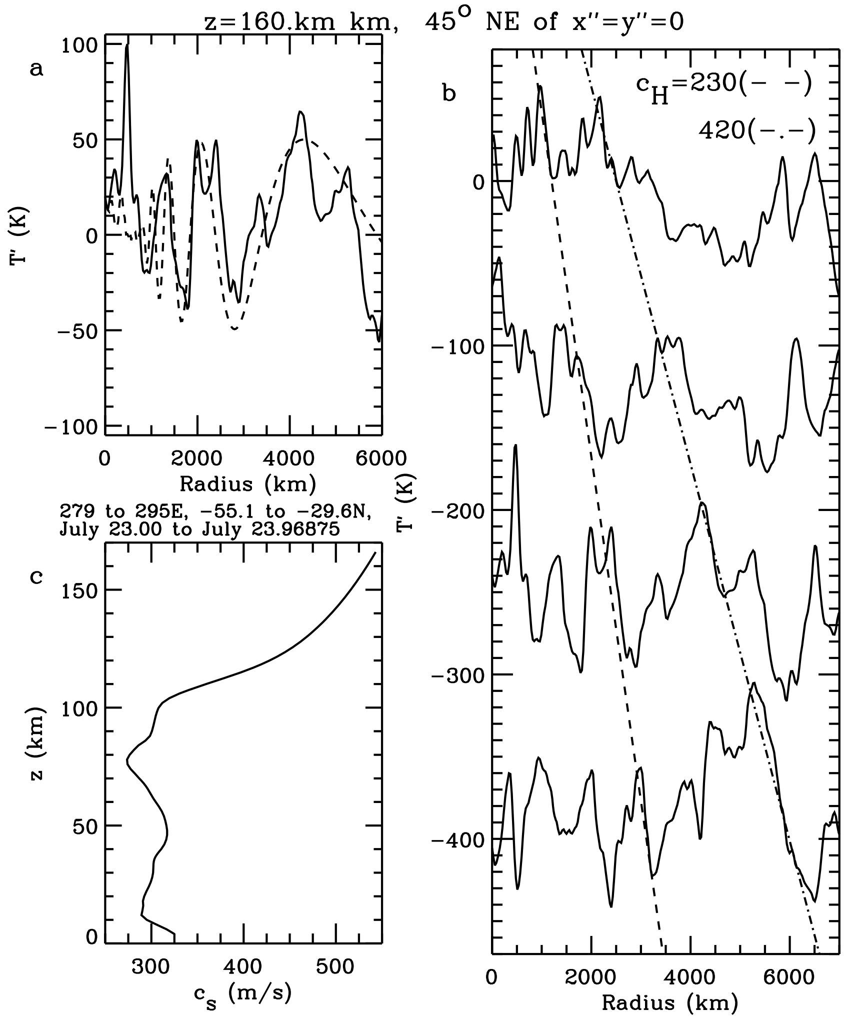

Figure 19. (a) T' (in K) at z = 160 km on 23.4375 July on a line 45° northeast from 300° E and 50° S (solid line). The dash line is given by equation (13), smoothed over 165 km. (b) T' (in K) every 45 min from 23.375 to 23.46875 July (upper to lower profiles) at z = 160 km on a line 45° northeast from 300° E and 50° S (solid line). The T' profiles are offset by 130 K. Dash and dash-dot lines show the locations of gravity waves propagating northeastward at horizontal phase speeds of 230 and 420 m/s, respectively. (c) c_s (in m/s) as a function of altitude, where c_s is averaged over 279 to 295° E and 55.1 to 29.6° S every 45 min from 23.0 to 23.96875 July.

where $k_H = 2\pi/\lambda_H$, λ_H is given by equation (12), and the subscript "ps" stands for point source. Here we smooth T'_{ps} over ≃165 km to account for the horizontal resolution of the KMCM. Additionally, we set $A = 50$ K, $\phi = 2.0$ rad, $c_z = 0.45$ m/s, $\tau_B = 8.31$ min, and $\Delta z = 30$ km, which corresponds to a point source at $z = 130$ km. We see that equation (13) agrees very well with T' for the larger-scale GWs.

Figure 19b shows T' every 45 min from 9:00 to 11:15 UT on 23 July at $z = 160$ km on a line 45° northeast from 300° E and 50° S (i.e., starting at $x'' = y'' = 0$) in the (x'', y'') 2-D plane. These GWs are the large-scale tertiary GWs propagating toward Africa in Figure 14f. We follow two wave packets here. The slower packet at smaller radii has an inferred ground-based horizontal phase speed of $c_H \simeq 230$ m/s. The faster wave packet at larger radii has a much larger inferred phase speed of $c_H \simeq 420$ m/s. These latter GWs have $\lambda_H \sim$ 2,000 km and $\tau_r = \lambda_H/c_H \sim 1.3$ hr. From Figures 16e and 16f, the background wind is $\bar{U} \sim -50$ m/s and $\bar{V} \sim -50$ m/s, which yields $U_H = -70$ m/s for the northeastward-propagating tertiary GWs. Therefore, their intrinsic horizontal phase speeds are $c_{IH} = c_H - U_H \simeq 490$ m/s, which is quite large. Figure 19c shows the mean sound speed, c_s, as a function of altitude. At $z = 160$ km, $c_s \simeq 535$ m/s. Therefore, $c_{IH} < c_s$ for these fast tertiary GWs at $z = 160$ km, as must be the case. This is because the maximum intrinsic horizontal phase speed that a GW can have is $c_{IH} < c_s$ (Vadas et al., 2019).

The result that some of the tertiary GWs have $c_H \simeq 420$ m/s is very important. This is because such fast GWs *cannot* propagate in the lower or middle atmosphere. This is because the sound speed below the turbopause is $c_s = 275$–300 m/s (see Figure 19c). Therefore, these GWs could have only been created in the thermosphere through the multistep vertical coupling mechanism from primary to secondary to tertiary GWs.

4.5. Potential Energy Density of the GWs

The potential energy density per unit mass for the GWs (PE) is

$$\mathrm{PE} = \frac{1}{2}\left(\frac{g}{N_B}\right)^2 \left(\frac{T'}{\bar{T}}\right)^2. \tag{14}$$

We compute the PE over the Southern Andes during the 23 July event. Here we approximate

$$N_B{}^2 \simeq g^2/(C_p\bar{T}), \tag{15}$$

where $C_p = \gamma \mathrm{r}/(\gamma - 1)$, $\mathrm{r} = 8,308/\mathrm{X_{MW}}$ m^2/s^2/K, $\mathrm{X_{MW}}$ is the mean molecular weight of the particle in the gas (in grams per mole), and g is the gravitational constant. For γ and $\mathrm{X_{MW}}$, we use empirical expressions (Equation (3)–(4) of Vadas, 2007)

$$\mathrm{X_{MW}} = \frac{1}{2}(\mathrm{X_{MW_0}} - \mathrm{X_{MW_1}})\left(1 - \tanh\left(\frac{\mathrm{s} - \mathrm{a}}{\Delta_a}\right)\right) + \mathrm{X_{MW_1}} \tag{16}$$

$$\gamma = \frac{1}{2}(\gamma_0 - \gamma_1)\left(1 - \tanh\left(\frac{\mathrm{s} - \mathrm{b}}{\Delta_b}\right)\right) + \gamma_1, \tag{17}$$

where $\mathrm{s} = -\ln(\bar{\rho})$ ($\bar{\rho}$ has units of grams per cubic meter), $\mathrm{X_{MW_0}} = 28.9$ grams/mole, $\mathrm{X_{MW_1}} = 16$ grams/mole, $\mathrm{a} = 14.9$, $\Delta_a = 4.2$, $\gamma_0 = 1.4$, $\gamma_1 = 1.67$, $\mathrm{b} = 15.1$, and $\Delta_b = 4.0$. The decrease of $\mathrm{X_{MW}}$ and increase of γ with altitude in the thermosphere represents the change from diatomic N_2 and O_2 to monatomic O.

Figure 20a shows the average PE as a function of altitude for the GWs (with periods $\tau_r \leq 11$ hr) over the Southern Andes on 23 July. Here we average the PE every 45 min from 0 to 23:15 UT over the region 279 to 295° E and 55.1 to 29.6° S. The PE is a complicated function of altitude. It increases with altitude up to $z \simeq 85$ km, decreases at $z \sim 85$–90 km, increases at $z \sim 90$–115 km, decreases at $z \sim 115$–125 km, and increases at $z \sim 125$–155 km. In the regions where the GWs are linear and nonattenuating and where the horizontal component of the background wind does not significantly refract the GWs (i.e., when the GW horizontal phase speeds are significantly larger than the horizontal background winds), we expect the PE to increase exponentially in altitude as $\exp(z/\mathcal{H}(z))$, because $T' \propto \exp(z/2\mathcal{H})$ in this case. To better understand and interpret the PE, we duplicate the PE in Figures 20b and 20c and overlay the following functions:

$$\alpha \int_{z_i}^{z} \exp(z'/\mathcal{H}(z'))dz', \tag{18}$$

where $\mathcal{H} = -\bar{\rho}/(d\bar{\rho}/dz)$ and $z_i = 4$ km. Here we choose the values of α such that equation (18) overlies the PE as closely as possible in the regions where the PE increases in altitude. We see that the PE increases exponentially in altitude up to $z \sim 55$ km (dashed line). This increase is slightly slower than given by equation (18). Since the PE shown in the figure is due to GW periods shorter than 11 hr, the stratospheric PE likely mainly contains inertia GWs that are generated in the troposphere from nonlinear baroclinic Rossby wave activity. These GWs can propagate in all directions relative to the mean wind. Those inertia GWs propagating mainly eastward and therefore parallel to the mean wind are attenuated from wave breaking triggered by convective (or dynamic) instability (as discussed for MWs in section 4.1) since the polar night jet increases with altitude in the stratosphere. Those GWs propagating mainly westward and therefore antiparallel to the mean wind are expected to be stabilized since their vertical wavelength increases with altitude. However, from the WKB solution for a medium-frequency GW, we have (e.g., Becker, 2004, his Equation (29))

$$w' \propto m^{-1/2}\exp(z/2H), \tag{19}$$

where $m = 2\pi/\lambda_z$; hence, the $PE \propto |m|\exp(z/H)$ from the polarization relation given by equation (11). Therefore, even a conservative GW shows an increase of PE in altitude that can be significantly weaker than $\exp(z/H)$ if $|\lambda_z|$ expands in altitude due to refraction by the background wind. The result shown in Figure 20c

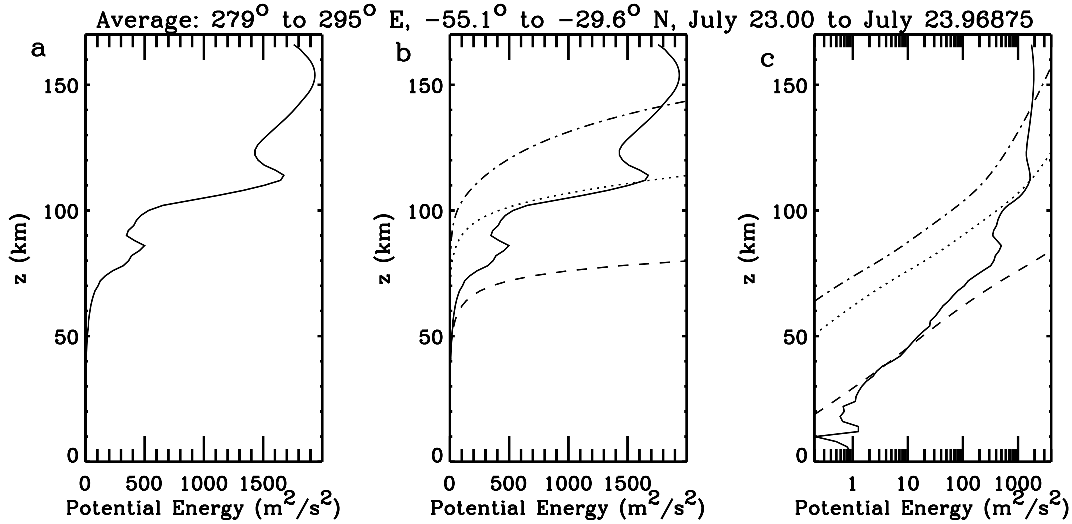

Figure 20. (a) Potential energy (PE) as a function of altitude (solid line). At each z, we average the PE every 45 min from 0 to 23:15 UT over the region 279 to 295° E and 55.1 to 29.6° S. (b) PE from (a) (solid line). We overlay $\alpha \int_{z_i}^{z} \exp(z'/\mathcal{H}(z'))dz'$, where $z_i = 4$ km, $\alpha = 0.02$ (dash line), $\alpha = 0.0002$ (dot line), $\alpha = 3.0 \times 10^{-5}$ (dash-dot line). (c) Same as (b) but with log scale on the x axis.

for the stratosphere presumably reflects a combination of these two mechanisms. The remaining westward inertia GWs then break in the lower mesosphere.

The slower-than-exponential increase of the PE at $z \sim 55$–85 km occurs where the smaller-amplitude secondary GWs are excited from MW breaking. In analogy to the inertia GWs in the stratosphere, these secondary GWs are subject to either refraction (for the predominantly eastward secondary GWs) or attenuation induced by refraction (for the predominantly westward secondary GWs) since the mean zonal wind decreases with altitude in the mesosphere. The PE increases exponentially according to $\exp(z/H)$ at $z \sim 95$–115 km (Figure 20b, dotted line); this is due to the growth of the secondary and smaller-amplitude tertiary GWs in a regime where the mean zonal wind does not change very much in altitude (see Figure 2). The decrease in the PE at $z \sim 115$–125 km occurs where most of the secondary GWs attenuate, which is strongly induced by the strong semidiurnal wind tide (BV18). Finally, although the PE increases at $z \sim 125$–160 km, it does not increase as rapidly as $\exp(z/H)$ (dashed-dotted line). This may be because (1) the tertiary GWs attenuate from parameterized diffusion and molecular diffusion there or (2) the tertiary GWs interact with the linear horizontal diffusion in the sponge layer soon after they are excited because $|\lambda_z|$ is very large.

5. Discussion

In this paper, we showed that the attenuation of MWs leads to the generation of secondary GWs, and their attenuation leads to the generation of tertiary GWs in the mesosphere and thermosphere. We show a sketch of the multistep vertical coupling mechanism in Figure 21. MWs are created from wind flow over orography. These MWs generate secondary GWs when they break/attenuate and create local body forces. These secondary GWs generate tertiary GWs when they break/attenuate in the mesosphere and thermosphere and create local body forces. These tertiary GWs then propagate to higher altitudes in the upper mesosphere and thermosphere before dissipating.

In the temporal and zonal-mean picture, this multistep vertical coupling leads to alternating signs of the GW drag. Figure 22a shows the temperature and the residual mass stream function, and Figure 22b shows the zonal wind and the Eliassen-Palm flux divergence from GWs having horizontal wavelengths shorter than ~1,350 km, denoted as GW drag. The GW drag changes from westward in the winter mesosphere to eastward above $z \sim 95$ km. It then changes to westward above $z \sim 130$ km over the southern polar cap. The eastward GW drag in the southern thermosphere is maximal at $z \sim 110$ km, 60° S and at $z \sim 160$ km, 45° S. The change in sign with increasing altitude above $z \sim 95$ km results from the breakdown of the secondary GWs. The change in sign above $z \sim 140$ km in winter toward a westward drag over the southern polar cap and the second eastward GW drag maximum at $z \sim 160$ km are due to tertiary GWs. These tertiary GWs are

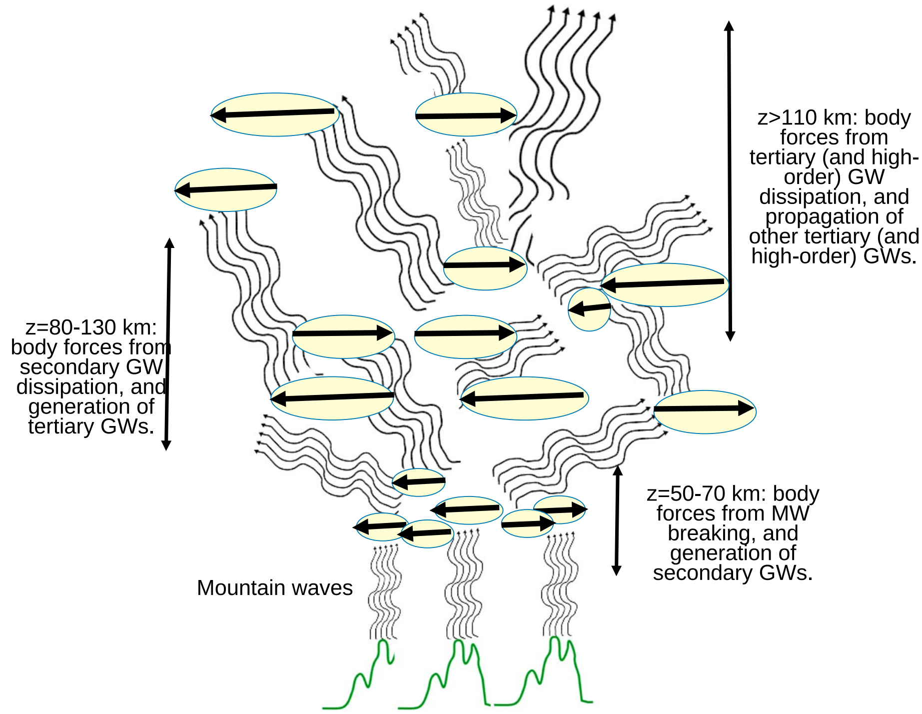

Figure 21. Schematic showing the vertical multistep coupling mechanism which links strong mountain wave events to tertiary (and higher-order) GWs in the thermosphere. Local body forces (horizontal black arrows) are created where the mountain waves break and attenuate at $z \sim 50$–70 km. Secondary GWs are generated by these body forces. The secondary GWs dissipate and create local body forces at $z \sim 80$–130 km, which generate tertiary GWs. Although many propagate to higher altitudes, some of the tertiary GWs begin to dissipate at $z > 110$ km. Only the upward-propagating secondary and tertiary GWs are shown here for clarity. (Not to scale). GW = gravity wave.

strongly damped by molecular diffusion and the sponge layer above ~165 km. Note that the Eliassen-Palm flux divergence due to GWs in the lower thermosphere is comparable in magnitude to that of the tides which is predominantly westward (not shown, see Becker, 2017).

For the 23 July event, we showed that some of the larger-scale tertiary GWs propagated northeastward to the western coast of Africa. The fastest of these wave packets had very large ground-based (intrinsic) horizontal phase speeds of $c_H \simeq 420$ m/s ($c_{IH} \simeq 490$ m/s) at $z = 160$ km (see Figure 19b). Because c_H minus the background wind is larger than the smallest value of the sound speed below $z \sim 100$ km, these GWs could not have been generated below $z \sim 100$ km. We now explain why this is so. The maximum intrinsic horizontal phase speed a GW can have is

$$max(c_{IH}) \simeq \frac{2\sqrt{\gamma - 1}}{\gamma} c_s \quad (20)$$

(Equation (35) of Vadas et al., 2019). Below the turbopause, $\gamma = 1.4$ because the atmosphere contains mainly diatomic molecules; then $max(c_{IH}) \simeq 0.90\,c_s$. The smallest value of c_s typically occurs at $z \sim 90$–100 km whereby $\bar{T}$ is a minimum, with $c_s \sim 260$–270 m/s. Therefore, a GW must have $c_{IH} < 230$–245 m/s (from equation (20)) in order to pass through this altitude range. Since $c_H = c_{IH} + U_H$ and the background wind is no larger than $U_H \sim 100$ m/s at $z \sim 90$–100 km from Figure 2, a GW that can pass through this altitude range must have $c_H < 330$–345 m/s. Therefore, the fast GWs with $c_H \sim 420$ m/s propagating toward Africa could not have been generated below $z \sim 100$ km. Instead, they must have been generated in the upper mesosphere or lower thermosphere (i.e., at $z > 100$ km) as tertiary GWs via the coupling mechanism shown in Figure 21. Note that because these fast GWs cannot propagate through the mesosphere, they also cannot be "launched" as parameterized GWs in the lower atmosphere; instead, they must be generated from momentum and energy deposition in the upper mesosphere and thermosphere.

Because the mechanism by which GWs are generated from local body forces is a fundamental physical process, it is clear that higher-order GWs will be generated where the tertiary GWs attenuate from molecular

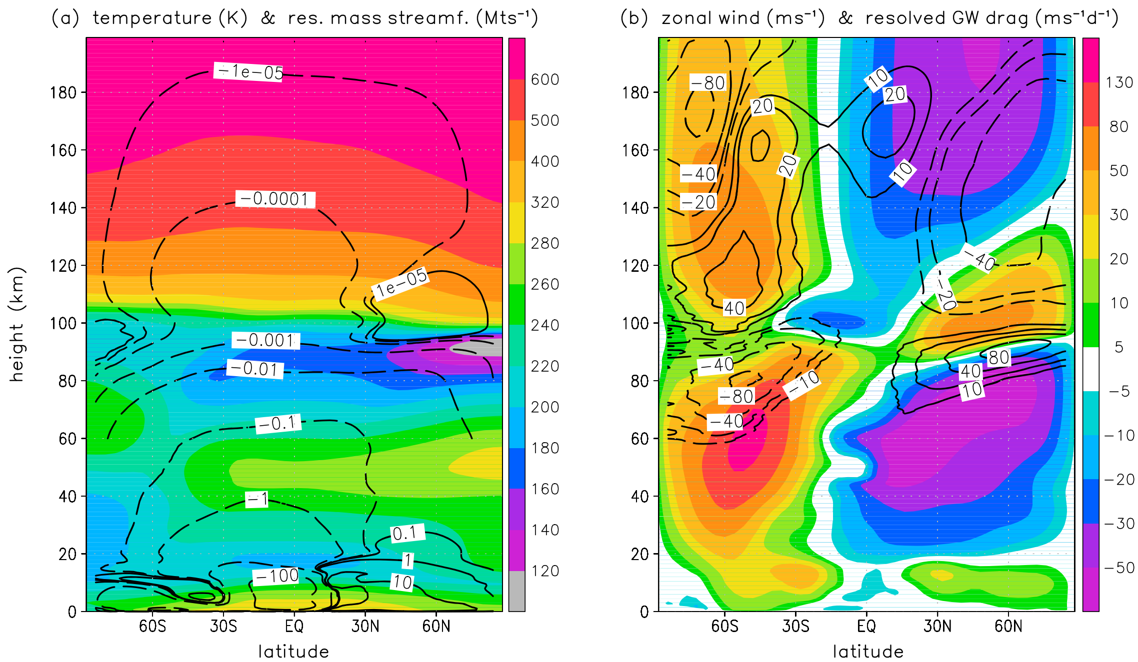

Figure 22. Zonal mean fields from the surface to 200 km. (a) Temperature (colors) and residual mass stream function (contours for $\pm 10^{-5}$, $\pm 10^{-4}$, ± 0.001, ± 0.01, ± 0.1, ± 1, ± 10, $+100$ Mt/s, 1 Mt $= 10^9$ kg). (b) Zonal wind (colors) and resolved gravity wave drag (contours for ± 10, ± 20, ± 40, ± 60, ± 80 m/s/day). The gravity wave drag is defined as the Eliassen-Palm flux divergence from horizontal wavelengths shorter than $\sim 1,350$ km.

viscosity (or breaking) and create local body forces. These higher-order GWs will then propagate to higher altitudes where they dissipate and create even higher-order GWs. Because the sound speed increases as $\sqrt{\bar{T}}$, some of these higher-order GWs will have larger intrinsic horizontal phase speeds, thereby enabling them to propagate to even higher altitudes in the thermosphere before dissipating from molecular viscosity (Vadas, 2007). In principle, this dissipation and generation process can occur over and over again until the generated GWs have large-enough c_{IH} to reach the highest altitudes in the thermosphere. This mechanism is likely the source of the quiettime "hotspot" traveling atmospheric disturbances observed over the Southern Andes in the middle and upper thermosphere (Forbes et al., 2016; Liu et al., 2017; Park et al., 2014; Trinh et al., 2018). Additionally, GWs have been observed in the 630.0-nm airglow in March over New Zealand; these GWs were identified as likely being secondary GWs from MW breaking (Smith et al., 2013).

Finally, we note that the model results we present in this paper (concerning the excitation and propagation of tertiary GWs over the wintertime Southern Andes) may have already been observed by others. In particular, Huang et al. (2017) observed a downward-propagating GW with $\lambda_H = 1,248$ km, $|\lambda_z| = 22$ km, and $\tau_r = 4.8$ hr at $z \sim 84$–102 km on 20–21 July 2015 at the Andes Lidar Observatory (ALO) in the Southern Andes (289.3° E and 30.3° S). This inertia GW was propagating northeastward at an azimuth of ~20° (east of north). Huang et al. (2017) argued that this GW could not have been a reflected GW but must have instead been created above 102 km. Because the horizontal and vertical wavelengths, period, and azimuth are similar to our model results, we infer that this GW was likely a downward-propagating tertiary GW, similar to the downward-propagating tertiary GWs at $z \simeq 90$–108 km in Figure 12. The local body force that created this GW must have been southwest of ALO, which is consistent with the location of some of the meridional body forces modeled here (see Figures 9g–9l). Simultaneously, Huang et al. (2017) also observed an upward-propagating GW with $\lambda_H = 935$ km, $|\lambda_z| = 10.9$ km, and $\tau_r = 5.4$ hr over the same altitude range. This inertia GW was propagating northwestward at an azimuth of approximately −23°. The authors reverse ray-traced this GW and found that it could have been created above the zonal wind jet that maximized at $z \sim 37$ km. The authors argued that this GW was likely created from the adjustment of the stratospheric jet. However, because secondary GWs are created above where the stratospheric jet maximizes (because $|\lambda_z|$ of the MWs decreases there, leading to convective instability via equation (7)) and because the horizontal and vertical wavelengths, period, and azimuth are similar to our model results, we suggest that this GW may have been an upward-propagating secondary GW. In this case, the local body force that created this GW would have been southeast of ALO, which is consistent with the location of most of the meridional body forces modeled here (see Figures 9a–9d). In order to determine the source of this latter GW, a detailed analysis of the MWs and the evolution of the background horizontal wind south of ALO would have to be made.

6. Conclusions

We used the high-resolution, GW-resolving KMCM to examine the effect that strong MW events over the wintertime Southern Andes have on the upper mesosphere and thermosphere. This model was recently extended so that the sponge layer sets in at $z \sim 165$ km. As is known from a previous study where the sponge layer began at $z \simeq 100$ km, (1) secondary GWs are generated near the stratopause where the MWs break and attenuate, and (2) many of these secondary GWs break and attenuate at $z < 100$ km (BV18). We find here that most of the secondary GWs actually dissipate in the upper mesosphere and lower thermosphere, thereby creating local body forces there. We find that these forces generate a broad spectrum of medium- and large-scale tertiary GWs that have partial concentric ring structure. While some of the tertiary GWs break and/or dissipate in the upper mesosphere and thermosphere, others freely propagate to $z \sim 170$ km.

We examined a strong orographic event on 23 July, during which MWs were created over the Southern Andes. These MWs propagated to $z \sim 50$–75 km, where they broke and attenuated. The largest-amplitude secondary GWs generated by this process were created by the MWs that were swept downstream (eastward) from the Southern Andes. These secondary GWs had partial concentric ring structures centered at $\simeq$300° E and $\simeq$60–65° S, with $\lambda_H \simeq 500$–$2{,}000$ km, $c_H \simeq 70$–100 m/s, and $\tau_r \simeq 3$–10 hr. Most of these secondary GWs are inertia GWs. Upon dissipation, these secondary GWs created a northeastward local body force with a very large amplitude of $\simeq$2,400 m/s/day over the South Atlantic Ocean at $z = 110$ km, $\simeq$300° E and $\simeq$50° S. This body force had a deep vertical extent of $z = 80$ to 130 km. We found that this force excited large-amplitude tertiary GWs with $\lambda_H \sim 350$–$2{,}000$ km and large $|\lambda_z|$ having stunning concentric ring structures. Most of these tertiary GWs had $c_H \simeq 120$–160 m/s, $\tau_r \sim 4$–9 hr, $u' \sim v' \sim 25$–50 m/s, $w' \sim 1$–10 m/s, $T' \sim 15$–25 K, and $\rho'/\bar{\rho} \sim 2$–10% at $z = 150$ km. We found that λ_H increased with radius from the ring centers and that this agreed well with the result for GWs excited by a point source. According to our model study, most of these tertiary GWs are inertia GWs.

We also examined the mean potential energy density PE during this event and found that it departed significantly from exponential at $z \sim 55$–80 km as a result of MW attenuation. This agrees with SABER and lidar observations (Lu et al., 2015, Liu et al., 2019; Preusse et al., 2006; Trinh et al., 2018). We found that the PE increased exponentially from $z \sim 95$ to 115 km because of the growth of the secondary and tertiary GWs, decreased at $z \simeq 115$–125 km because of the dissipation of most of the secondary GWs, and increased at $z \sim 125$–160 km because of the growth of the tertiary GWs. We showed that this multistep vertical coupling mechanism leads to alternating signs of the GW drag.

Some of the tertiary GWs in our model study had $c_H \sim 420$ m/s; we argued that these GWs could not have been generated below $z \sim 100$ km. This is an important result, because we found in our companion paper that most of the identified hot spot GWs extracted from GOCE over the Southern Andes on 5 July 2010 at $z = 277$ km were tertiary GWs with horizontal phase speeds in excess of 300 m/s (Vadas et al., 2019). Thus, this study shows that the KMCM simulates the previously unknown source mechanism for these fast, quiettime hot spot GOCE GWs.

We conclude that strong orographic forcing results in the excitation of fast medium- and large-scale GWs in the mesosphere and thermosphere through this complex multistep coupling mechanism from the troposphere to the thermosphere, as summarized in Figure 21. Because the neutrals move ions along the Earth's magnetic field, those tertiary and higher-order GWs that can propagate into the F region will create medium- and large-scale traveling ionospheric disturbances (Nicolls et al., 2014; Vadas & Nicolls, 2009), although it is expected that only those GWs having intrinsic periods smaller than a few hours (along with having large horizontal phase speeds) can achieve this (Vadas, 2007). This process may have important consequences for the variability of the ionosphere. Additionally, the background flow in the thermosphere will be altered where the tertiary and higher-order GWs attenuate, which could significantly change the large-scale circulation of the thermosphere.

Acknowledgments
We would like to thank the anonymous reviewers for helpful comments. S. L. V. was supported by NSF grants AGS-1832988 and AGS-1552315. E. B. was supported by the Collaborative Research Centre TRR 181 (subproject T1) funded by the German Research Foundation. The model data shown in this paper are available via NWRA's website (https://www.cora.nwra.com/vadas/Vadas_Becker_JGR_2019_files/).

References

Alexander, M. J., & Teitelbaum, H. (2007). Observation and analysis of a large amplitude mountain wave event over the Antarctic peninsula. *Journal of Geophysical Research*, *112*, D21103. https://doi.org/10.1029/2006JD008368

Alexander, M. J., & Teitelbaum, H. (2011). Three-dimensional properties of Andes mountain waves observed by satellite: A case study. *Journal of Geophysical Research*, *116*, D23110. https://doi.org/10.1029/2011JD016151

Alexander, M. J., Gille, J., Cavanaugh, C., Coffey, M., Craig, C., Eden, T., et al. (2008). Global estimates of gravity wave momentum flux from High Resolution Dynamics Limb Sounder Observations. *Journal of Geophysical Research*, *113*, D15S18. https://doi.org/10.1029/2010JD008807

Becker, E. (2004). Direct heating rates associated with gravity wave saturation. *Journal of Atmospheric and Terrestrial Physics*, *66*, 683–696.

Becker, E. (2009). Sensitivity of the upper mesosphere to the Lorenz energy cycle of the troposphere. *Journal of the Atmospheric Sciences*, *66*, 647–666. https://doi.org/10.1175/2008JAS2735.1

Becker, E. (2012). Dynamical control of the middle atmosphere. *Space Science Reviews*, *168*, 283–314. https://doi.org/10.1007/s11214-011-9841-5

Becker, E. (2017). Mean-flow effects of thermal tides in the mesosphere and lower thermosphere. *Journal of the Atmospheric Sciences*, *74*, 2043–2063. https://doi.org/10.1175/JAS-D-16-0194.1

Becker, E., Knöpfel, R., & Lübken, F.-J. (2015). Dynamically induced hemispheric differences in the seasonal cycle of the summer polar mesopause. *Journal of Atmospheric and Solar-Terrestrial Physics*, *129*, 128–141. https://doi.org/10.1016/j.jastp.2015.04.014

Becker, E., & Vadas, S. L. (2018). Secondary gravity waves in the winter mesosphere: Results from a high-resolution global circulation model. *Journal of Geophysical Research: Atmospheres*, *123*, 2605–2627. https://doi.org/10.1002/2017JD027460

Bossert, K., Fritts, D. C., Pautet, P.-D., Williams, B. P., Taylor, M. J., Kaifler, B., et al. (2015). Momentum flux estimates accompanying multiscale gravity waves over Mount Cook, New Zealand, on 13 July 2014 during the DEEPWAVE campaign. *Journal of Geophysical Research: Atmospheres*, *120*, 9323–9337. https://doi.org/10.1002/2015JD023197

Bossert, K., Kruse, C. G., Heale, C. J., Fritts, D. C., Williams, B. P., Snively, J. B., et al. (2017). Secondary gravity wave generation over New Zealand during the DEEPWAVE campaign. *Journal of Geophysical Research: Atmospheres*, *122*, 7834–7850. https://doi.org/10.1002/2016JD026079

Bruinsma, S. L., & Forbes, J. M. (2008). Medium to large-scale density variability as observed by CHAMP. *Space Weather*, *6*, S08002. https://doi.org/10.1029/2008SW000411

Brune, S., & Becker, E. (2013). Indications of stratified turbulence in a mechanistic GCM. *Journal of the Atmospheric Sciences*, *70*, 231–247. https://doi.org/10.1175/JAS-D-12-025.1

Chen, C., & Chu, X. (2017). Two-dimensional Morlet wavelet transform and its application to wave recognition methodology of automatically extracting two-dimensional wave packets from lidar observations in Antarctica. *Journal of Atmospheric and Solar-Terrestrial Physics*, *162*, 28–47. https://doi.org/10.1016/j.jastp.2016.10.016

Chen, C., Chu, X., McDonald, A. J., Vadas, S. L., Yu, Z., Fong, W., & Lu, X. (2013). Inertia-gravity waves in Antarctica: A case study using simultaneous lidar and radar measurements at McMurdo/Scott Base (77.8° S, 166.7° E). *Journal of Geophysical Research: Atmospheres*, *118*, 2794–2808. https://doi.org/10.1002/jgrd.50318

de Wit, R. J., Janches, D., Fritts, D. C., Stockwell, R., & Coy, L. (2017). Unexpected climatological behavior of MLT gravity wave momentum flux in the lee of the southern Andes hotspot. *Geophysical Research Letters*, *4*, 1172–1191. https://doi.org/10.1002/2016GL072311

de la Torre, A., & Alexander, P. (2005). Gravity waves above Andes detected from GPS radio occultation temperature profiles: Mountain forcing? *Geophysical Research Letters*, *32*, L17815. https://doi.org/10.1029/2005GL022959

DelGenio, A. D., & Schubert, G. (1979). Gravity wave propagation in a diffusively separated atmosphere with height-dependent collision frequencies. *Journal of Geophysical Research*, *84*, 4371–4378.

Djuth, F. T., Sulzer, M. P., Elder, J. H., & Wickwar, V. B. (1997). High-resolution studies of atmosphere-ionosphere coupling at Arecibo Observatory, Puerto Rico. *Radio Science*, *32*, 2321–2344.

Djuth, F. T., Sulzer, M. P., Gonzales, S. A., Mathews, J. D., Elder, J. H., & Walterscheid, R. L. (2004). A continuum of gravity waves in the Arecibo thermosphere? *Geophysical Research Letters*, *31*, L16801. https://doi.org/10.1029/2003GL019376

Eckermann, S. D., Broutman, D., Ma, J., Doyle, J. D., Pautet, P.-D., Taylor, M. J., et al. (2016). Dynamics of orographic gravity waves observed in the mesosphere over the Auckland islands during the Deep Propagating Gravity Wave Experiment (DEEPWAVE). *Journal of the Atmospheric Sciences*, *73*, 3855–3876. https://doi.org/10.1175/JAS-D-16-0059.1

Eckermann, S. D., & Preusse, P. (1999). Global measurements of stratospheric mountain waves from space. *Science*, *286*(5444), 1534–1537. https://doi.org/10.1126/science.286.5444.1534

Ern, M., Preusse, P., Alexander, M. J., & Warner, C. D. (2004). Absolute values of gravity wave momentum flux derived from satellite data. *Journal of Geophysical Research*, *109*, D20103. https://doi.org/10.1029/2004JD004752

Ern, M., Preusse, P., Gille, J. C., Hepplewhite, C. L., Mlynczak, M. G., J. M. Russell III, & Riese, M. (2011). Implications for atmospheric dynamics derived from global observations of gravity wave momentum flux in stratosphere and mesosphere. *Journal of Geophysical Research*, *116*, D19107. https://doi.org/10.1029/2011JD015821

Forbes, J. M., Bruinsma, S. L., Doornbos, E., & Zhang, X. (2016). Gravity wave-induced variability of the middle thermosphere. *Journal of Geophysical Research: Space Physics*, *121*, 6914–6923. https://doi.org/10.1002/2016JA022923

Fritts, D. C., & Alexander, M. J. (2003). Gravity wave dynamics and effects in the middle atmosphere. *Reviews of Geophysics*, *41*(1), 1003. https://doi.org/10.1029/2001RG000106

Fritts, D. C., Smith, R. B., Taylor, M. J., Doyle, J. D., Eckermann, S. D., Dörnbrack, A., et al. (2016). The Deep Propagating Gravity Wave Experiment (DEEPWAVE): An airborne and ground-based exploration of gravity wave propagation and effects from their sources throughout the lower and middle atmosphere. *Bulletin of the American Meteorological Society*, *97*, 425–453. https://doi.org/10.1175/BAMS-D-14-00269.1

Fritts, D. C., Vadas, S. L., Wan, K., & Werne, J. A. (2006). Mean and variable forcing of the middle atmosphere by gravity waves. *Journal of Atmospheric and Solar-Terrestrial Physics*, *68*, 247–265.

Gong, J., Wu, D. L., & Eckermann, S. D. (2012). Gravity wave variances and propagation derived from AIRS radiances. *Atmospheric Chemistry and Physics*, *12*, 1701–1720. https://doi.org/10.5194/acp-12-1701-2012

Gossard, E. E., & Hooke, W. H. (1975). *Waves in the atmosphere* (pp. 456). New York: Elsevier Scientific Publishing Co.

Heale, C. J., Bossert, K., Snively, J. B., Fritts, D. C., Pautet, P.-D., & Taylor, M. J. (2017). Numerical modeling of a multiscale gravity wave event and its airglow signatures over Mount Cook, New Zealand, during the DEEPWAVE campaign. *Journal of Geophysical Research: Space Physics*, *122*, 846–860. https://doi.org/10.1002/2016JD025700

Hedin, A. E., & Mayr, H. G. (1987). Characteristics of wavelike fluctuations in Dynamics Explorer neutral composition data. *Journal of Geophysical Research*, *92*, 11,159–11,172.

Hendricks, E. A., Doyle, J. D., Eckermann, S. D., Jiang, Q., & Reinecke, P. A. (2014). What is the source of the stratospheric gravity wave belt in austral winter? *Journal of the Atmospheric Sciences*, *71*, 1583–1592. https://doi.org/10.1175/JAS-D-13-0332.1

Hickey, M. P., & Cole, K. D. (1988). A numerical model for gravity wave dissipation in the thermosphere. *Journal of Atmospheric and Solar-Terrestrial Physics*, *50*, 689–697.

Hines, C. O. (1960). Internal atmospheric gravity waves at ionospheric heights. *Canadian Journal of Physics*, *38*, 1441–1481.

Hoffmann, L., & Alexander, M. J. (2009). Retrieval of stratospheric temperatures from Atmospheric Infrared Sounder radiance measurements for gravity wave studies. *Journal of Geophysical Research*, *114*, D07105. https://doi.org/10.1029/2008JD011241

Hoffmann, L., Xue, X., & Alexander, M. J. (2013). A global view of stratospheric gravity wave hotspots located with Atmospheric Infrared Sounder observations. *Journal of Geophysical Research: Space Physics*, *118*, 416–434.

Holton, J. R. (1992). *An introduction to dynamic meteorology* (pp. 507). San Diego, CA: Academic Press.

Hong, S.-S., & Lindzen, R. S. (1976). Solar semidiurnal tide in the thermosphere. *Journal of the Atmospheric Sciences*, *33*, 135–153.

Huang, K. M., Liu, A. Z., Zhang, S. D., Yi, F., Huang, C. M., Gong, Y., et al. (2017). Simultaneous upward and downward propagating inertia-gravity waves in the MLT observed at Andes Lidar Observatory. *Journal of Geophysical Research: Atmospheres*, *122*, 2812–2830. https://doi.org/10.1002/2016JD026178

Jiang, J. H., Wu, D. L., & Eckermann, S. D. (2002). Upper Atmosphere Research Satellite (UARS) MLS observation of mountain waves over the Andes. *Journal of Geophysical Research*, *107*(D20), 8273. https://doi.org/10.1029/2002JD002091

Lindzen, R. S. (1981). Turbulence and stress owing to gravity wave and tidal breakdown. *Journal of Geophysical Research*, *86*(C10), 9707–9714.

Liu, H., Pedatella, N., & Hocke, K. (2017). Medium-scale gravity wave activity in the bottomside F region in tropical regions. *Geophysical Research Letters*, *44*, 7099–7105. https://doi.org/10.1002/2017GL073855

Liu, X., Xu, J., Yue, J., Vadas, S. L., & Becker, E. (2019). Orographic primary and secondary gravity waves in the middle atmosphere from 16-year SABER observations. *Geophysical Research Letters*, *46*, 4512–4522. https://doi.org/10.1029/2019GL082256

Lu, X., Chu, X., Fong, W., Chen, C., Yu, Z., Roberts, B. R., & McDonald, A. J. (2015). Vertical evolution of potential energy density and vertical wave number spectrum of Antarctic gravity waves from 35 to 105 km at McMurdo (77.8°S, 166.7°E). *Journal of Geophysical Research: Atmospheres*, *120*, 2719–2737. https://doi.org/10.1002/2014JD022751

Lund, T. S., & Fritts, D. C. (2012). Numerical simulation of gravity wave breaking in the lower thermosphere. *Journal of Geophysical Research*, *117*, D21105. https://doi.org/10.1029/2012JD017536

Mayr, H. G., Harris, I., Herrero, F. A., Spencer, N. W., Varosi, F., & Pesnell, W. D. (1990). Thermospheric gravity waves: Observations and interpretation using the transfer function model (TEM). *Space Science Reviews*, *54*, 297–375.

McFarlane, N. A. (1987). The effect of orographically excited gravity wave drag on the general circulation of the lower stratosphere and troposphere. *Journal of the Atmospheric Sciences*, *44*, 1775–1800.

Miyoshi, Y., & Fujiwara, H. (2008). Gravity waves in the thermosphere simulated by a general circulation model. *Journal of Geophysical Research*, *113*, D01101. https://doi.org/10.1029/2007JD008874

Nicolls, M. J., Vadas, S. L., Aponte, N., & Sulzer, M. P. (2014). Horizontal wave parameters of daytime thermospheric gravity waves and E region neutral winds over Puerto Rico. *Journal of Geophysical Research: Space Physics*, *119*, 576–600. https://doi.org/10.1002/2013JA018988

Oliver, W. L., Otsuka, Y., Sato, M., Takami, T., & Fukao, S. (1997). A climatology of F region gravity wave propagation over the middle and upper atmosphere radar. *Journal of Geophysical Research*, *102*, 14,499–14,512.

Park, J., Lühr, H., Lee, C., Kim, Y. H., Jee, G., & Kim, J.-H. (2014). A climatology of medium-scale gravity wave activity in the midlatitude/low-latitude daytime upper thermosphere as observed by CHAMP. *Journal of Geophysical Research: Space Physics*, *119*, 2187–2196. https://doi.org/10.1002/2013JA019705

Pitteway, M. L. V., & Hines, C. O. (1963). The viscous damping of atmospheric gravity waves. *Canadian Journal of Physics*, *41*, 1935–1948.

Plougonven, R., Hertzog, A., & Teitelbaum, H. (2008). Observations and simulations of a large-amplitude mountain wave breaking over the Antarctic Peninsula. *Journal of Geophysical Research*, *113*, D16113. https://doi.org/10.1029/2007JD009739

Preusse, P., Dörnbrack, A., Eckermann, S. D., Riese, M., Schaeler, B, Bacmeister, J. T., et al. (2002). Space-based measurements of stratospheric mountain waves by CRISTA. 1. Sensitivity analysis method, and a case study. *Journal of Geophysical Research*, *107*, 8178. https://doi.org/10.1029/2001JD000699

Preusse, P., Ern, M., Eckermann, S. D., Warner, C. D., Picard, R. H., Knieling, P., et al. (2006). Tropopause to mesopause gravity waves in August: Measurement and modeling. *Journal of Atmospheric and Solar-Terrestrial Physics*, *68*, 1730–1751.

Sato, K., Tateno, S., Watanabe, S., & Kawatani, Y. (2012). Gravity wave characteristics in the Southern Hemisphere revealed by a high-resolution middle-atmosphere general circulation model. *Journal of the Atmospheric Sciences*, *69*, 1378–1396. https://doi.org/10.1175/JAS-D-11-0101.1

Smith, S., Baumgardner, J., & Mendillo, M. (2009). Evidence of mesospheric gravity-waves generated by orographic forcing in the troposphere. *Geophysical Research Letters*, *36*, L08807. https://doi.org/10.1029/2008GL036936

Smith, S. M., Vadas, S. L., Baggaley, W. J., Hernandez, G., & Baumgardner, J. (2013). Gravity wave coupling between the mesosphere and thermosphere over New Zealand. *Journal of Geophysical Research: Space Physics*, *118*, 2694–2707. https://doi.org/10.1002/jgra.50263

Trinh, Q. T., Ern, M., Doornbos, E., Preusse, P., & Riese, M. (2018). Satellite observations of middle atmosphere-thermosphere vertical coupling by gravity waves. *Annales Geophysicae*, *36*, 425–444. https://doi.org/10.5194/angeo-36-425-2018

Tsuda, T., Nishida, M., Rocken, C., & Ware, R. H. (2000). A global morphology of gravity wave activity in the stratosphere revealed by the GPS occultation data (GPS/MET). *Journal of Geophysical Research*, *105*, 7257–7273.

Vadas, S. L. (2007). Horizontal and vertical propagation and dissipation of gravity waves in the thermosphere from lower atmospheric and thermospheric sources. *Journal of Geophysical Research*, *112*, A06305. https://doi.org/10.1029/2006JA011845

Vadas, S. L. (2013). Compressible f -plane solutions to body forces, heatings, and coolings, and application to the primary and secondary gravity waves generated by a deep convective plume. *Journal of Geophysical Research: Space Physics*, *118*, 2377–2397. https://doi.org/10.1002/jgra.50163

Vadas, S. L., & Becker, E. (2018). Numerical modeling of the excitation, propagation, and dissipation of primary and secondary gravity waves during wintertime at McMurdo Station in the Antarctic. *Journal of Geophysical Research: Atmospheres*, *123*, 9326–9369. https://doi.org/10.1029/2017JD027974

Vadas, S. L., & Crowley, G. (2010). Sources of the traveling ionospheric disturbances observed by the ionospheric TIDDBIT sounder near Wallops Island on October 30, 2007. *Journal of Geophysical Research*, *115*, A07324. https://doi.org/10.1029/2009JA015053

Vadas, S. L., & Fritts, D. C. (2001). Gravity wave radiation and mean responses to local body forces in the atmosphere. *Journal of the Atmospheric Sciences*, *58*, 2249–2279.
Vadas, S. L., & Fritts, D. C. (2002). The importance of spatial variability in the generation of secondary gravity waves from local body forces. *Geophysical Research Letters*, *29*(20), 1984. https://doi.org/10.1029/2002GL015574
Vadas, S. L, & Fritts, D. C. (2004). Thermospheric responses to gravity waves arising from mesoscale convective complexes. *Journal of Atmospheric and Solar-Terrestrial Physics*, *66*, 781–804.
Vadas, S. L., & Fritts, D. C. (2005). Thermospheric responses to gravity waves: Influences of increasing viscosity and thermal diffusivity. *Journal of Geophysical Research*, *110*, D15103. https://doi.org/10.1029/2004JD005574
Vadas, S. L., Fritts, D. C., & Alexander, M. J. (2003). Mechanism for the generation of secondary waves in wave breaking regions. *Journal of the Atmospheric Sciences*, *60*, 194–214.
Vadas, S. L., & Liu, H.-L. (2009). The generation of large-scale gravity waves and neutral winds in the thermosphere from the dissipation of convectively-generated gravity waves. *Journal of Geophysical Research*, *114*, A10310. https://doi.org/10.1029/2009JA014108
Vadas, S. L., & Liu, H.-L. (2013). Numerical modeling of the large-scale neutral and plasma responses to the body forces created by the dissipation of gravity waves from 6 h of deep convection in Brazil. *Journal of Geophysical Research: Space Physics*, *118*, 2593–2617. https://doi.org/10.1002/jgra.50249
Vadas, S. L., Liu, H.-L., & Lieberman, R. S. (2014). Numerical modeling of the global changes to the thermosphere and ionosphere from the dissipation of gravity waves from deep convection. *Journal of Geophysical Research: Space Physics*, *119*, 7762–7793. https://doi.org/10.1002/2014JA020280
Vadas, S. L., & Nicolls, M. J. (2009). Temporal evolution of neutral, thermospheric winds and plasma response using PFISR measurements of gravity waves. *Journal of Atmospheric and Solar-Terrestrial Physics*, *71*, 740–770.
Vadas, S. L., & Nicolls, M. J. (2012). The phases and amplitudes of gravity waves propagating and dissipating in the thermosphere: Theory. *Journal of Geophysical Research*, *117*, A05322. https://doi.org/10.1029/2011JA017426
Vadas, S. L., Xu, S., Yue, J., Bossert, K., Becker, E., & Baumgarten, G. (2019). Characteristics of the quiet-time hotspot gravity waves observed by GOCE over the Southern Andes on 5 July 2010. *Journal of Geophysical Research: Space Physics*. https://doi.org/10.1029/2019JA026693
Vadas, S. L., Zhao, J., Chu, X., & Becker, E. (2018). The excitation of secondary gravity waves from local body forces: Theory and observation. *Journal of Geophysical Research: Atmospheres*, *123*, 9296–9325. https://doi.org/10.1029/2017JD027970
Vincent, R. A., Hertzog, A., Boccara, G., & Vial, F. (2007). Quasi-Lagrangian superpressure balloon measurements of gravity-wave momentum fluxes in the polar stratosphere of both hemispheres. *Geophysical Research Letters*, *34*, L19804. https://doi.org/10.1029/2007GL031072
Volland, H. (1969). Full wave calculations of gravity wave propagation through the thermosphere. *Journal of Geophysical Research*, *74*, 1786–1795.
Walterscheid, R. L., Gelinas, L. J., Mechoso, C. R., & Schubert, G. (2016). Spectral distribution of gravity wave momentum fluxes over the Antarctic Peninsula from Concordiasi superpressure balloon data. *Journal of Geophysical Research: Atmospheres*, *121*, 7509–7527. https://doi.org/10.1002/2015JD024253
Watanabe, S., Sato, K., & Takahashi, M. (2006). A general circulation model study of orographic gravity waves over Antarctica excited by katabatic winds. *Journal of Geophysical Research*, *111*, D18104. https://doi.org/10.1029/2005JD006851
Wu, D. L., & Eckermann, S. D. (2008). Global gravity wave variances from Aura MLS: Characteristics and interpretation. *Journal of the Atmospheric Sciences*, *65*, 3695–3718. https://doi.org/10.1175/2008JAS2489.1
Wu, D. L., & Jiang, J. H. (2002). MLS observations of atmospheric gravity waves over Antarctica. *Journal of Geophysical Research*, *107*(D24), 4773. https://doi.org/10.1029/2002JD002390
Wu, D. L., Preusse, P., Eckermann, S. D., Jiang, J. H., de la, M., Juarez, T., et al. (2006). Remote sounding of atmospheric gravity waves with satellite limb and nadir techniques. *Advances in Space Research*, *37*, 2269–2277. https://doi.org/10.1016/j.asr.2005.07.031
Yiğit, E., Aylward, A. D., & Medvedev, A. S. (2008). Parameterization of the effects of vertically propagating gravity waves for thermosphere general circulation models: Sensitivity study. *Journal of Geophysical Research*, *113*, D19106. https://doi.org/10.1029/2008JD010135
Yiğit, E., Medvedev, A. S., Aylward, A. D., Hartogh, P., & Harris, M. J. (2009). Modeling the effects of gravity wave momentum deposition on the general circulation above the turbopause. *Journal of Geophysical Research*, *114*, D07101. https://doi.org/10.1029/2008JD011132
Zhao, J., Chu, X., Chen, C., Lu, X., Fong, W., Yu, Z., et al. (2017). Lidar observations of stratospheric gravity waves from 2011 to 2015 at McMurdo (77.84° S, 166.69° E), Antarctica: Part I. Vertical wavelengths, periods, and frequency and vertical wavenumber spectra. *Journal of Geophysical Research: Space Physics*, *122*, 5041–5062. https://doi.org/10.1002/2016JD026368